Photocatalytic degradation of bacterial lipopolysaccharides by peptide-coated TiO_2 nanoparticles

Lucrezia Caselli[1,*], *Guanqun Du*[1], *Samantha Micciulla*[2], *Tanja Traini*[3], *Federica Sebastiani*[1,3], *Ragna Guldsmed Diedrichsen*[3], *Sebastian Köhler*[4], *Maximilian W. A. Skoda*[5], *Mariena J.A. van der Plas*[3], *and Martin Malmsten*[1,3]

[1]Department of Physical Chemistry 1, Lund University, SE-22100 Lund, Sweden

[2]Institut Laue–Langevin, CS 20156, 38042 Grenoble Cedex 9, France

[3]Department of Pharmacy, University of Copenhagen, DK-2100 Copenhagen, Denmark

[4]LINXS Institute of Advanced Neutron and X-ray Science, Scheelevagen 19, 22370 Lund, Sweden

[5]ISIS Pulsed Neutron and Muon Source, Rutherford Appleton Laboratory, OX11 0QX, Harwell, UK

[*]Corresponding author

KEYWORDS: Antimicrobial peptide, lipopolysaccharide, photocatalysis, oxidation, TiO_2

Abstract

In the present study, we investigated the degradation of both smooth and rough lipopolysaccharides from Gram-negative (LPS) and lipoteichoic acid from Gram-positive (LTA) bacteria by peptide-coated TiO_2 nanoparticles (TiO_2 NPs). While bare TiO_2 NPs displayed minor binding to both LPS and LTA, coating TiO_2 NPs with the antimicrobial peptide LL-37 dramatically increased binding to LPS and LTA, decorating these uniformly. Importantly, peptide coating did not suppress reactive oxygen species generation of TiO_2 NPs, hence UV illumination triggered pronounced degradation of LPS and LTA by peptide-coated TiO_2 NPs. Structural aspects of oxidative degradation were investigated by neutron reflectometry for smooth LPS, showing that degradation occurred preferentially in its outer O-antigen tails. Furthermore, cryo-TEM and light scattering showed lipopolysaccharide fragments resulting from degradation to be captured by the NP/LPS co-aggregates. The ability of LL-37-TiO_2 NPs to capture and degrade LPS and LTA was demonstrated to be of importance for their ability to suppress lipopolysaccharide-induced activation in human monocytes at simultaneously low toxicity. Together, these results suggest that peptide-coated photocatalytic NPs offer opportunities for confinement of infection and inflammation.

Introduction

As a result of antibiotics resistance development, bacterial infections are on their way to once again become a leading cause of severe illness and death, also in developed countries (1,2). It is therefore urgent to develop novel antimicrobial therapeutics. Besides drugs, nanomaterials may display potent antimicrobial properties, also against strains resistant to antibiotics (3-5). Among nanomaterials, those displaying photocatalytic activity currently attract considerable interest. In photocatalysis, light triggers formation of excited electrons and holes, which may react with water, dissolved oxygen, or solutes to form reactive oxygen species (ROS) at the nanoparticle surface. ROS are highly reactive and may degrade essential bacteria components, such as phospholipids, lipopolysaccharides, proteins, or DNA (6). As a result, photocatalytic nanoparticles (NPs) may display potent antimicrobial effects (7,8). However, the mechanistic understanding of such effects remains elusive and further work is needed to clarify how antimicrobial effects and toxicity depend on bacteria membrane composition.

Compared to human cells, bacterial membranes are rich in anionic phospholipids and do not contain any sterols (11-14). In addition, bacterial membranes are rich in bacterial lipopolysaccharides. Thus, LPS dominates the outer membrane of Gram-negative bacteria (15), whereas lipoteichoic acid (LTA) is abundant in the peptidoglycan layer of Gram-positive bacteria (16). (As LTA also belongs to the family of lipopolysaccharides, both LPS from Gram-negative bacteria and LTA are generically referred to as "lipopolysaccharides" throughout the manuscript.) Due to their amphiphilicity and net negative charge, lipopolysaccharides interact strongly with cationic and amphiphilic compounds, such as antimicrobial peptides (AMPs) (17,18). In fact, AMP binding to bacterial lipopolysaccharides plays a key role for both antimicrobial and anti-inflammatory effects of such peptides (19-21). Considering the pronounced lipopolysaccharide binding of AMPs, coating photocatalytic NPs with AMPs may thus represent an interesting approach for effectively targeting such nanomaterials towards bacterial membranes.

Recently, we reported on the coating photocatalytic NPs by AMPs for selective oxidative degradation of bacteria-like membranes. In doing so, we found that peptide coating enhanced binding to bacteria-like phospholipid bilayers, and caused selective degradation of these, as well as boosted antimicrobial effects while simultaneously exerting low toxicity against human cells (22). Investigating how such effects depend on the properties of peptides used for nanoparticle coating, we very recently compared effects of the AMP KYE21 and its hydrophobized WWWKYE21 variant, showing that: (i) peptide-

coated TiO_2 nanoparticles displayed similar binding selectivity between bacteria- and cell-mimicking model membranes as the free peptides, (ii) binding of WWWKYE21-TiO_2 to bacteria-like membranes was higher than that of KYE21-TiO_2, as were antimicrobial effects, but also (iii) that saturation in photocatalytic effects occurs at very high nanoparticle binding density due to light scattering (23).

While the latter study indicated favorable effects of AMP-coating of photocatalytic nanoparticles for LPS degradation, further work is needed since little is known about lipopolysaccharide structure on its degradation by photocatalytic NPs, and about consequences of lipopolysaccharide degradation for cell activation and inflammation (18). Thus, while complete degradation of lipopolysaccharides can be expected to result in efficient suppression of cell activation, lipopolysaccharide fragments released during the degradation process may still be inflammatory. Incomplete lipopolysaccharide degradation and/or residue capture may therefore aggravate the situation, analogous to inflammation triggered by *Klebsiella pnumoniae* on inappropriate antibiotics exposure (24). Addressing this knowledge gap, we set out in the present study to address the following research questions: (i) How does oxidative degradation of bacterial lipopolysaccharides depend on their structure?; (ii) Can oxidative degradation of bacterial lipopolysaccharides be boosted by AMP-coating of photocatalytic NPs?; (iii) How does this translate into anti-inflammatory effects and cell toxicity?

In doing so, we focus on TiO_2 NPs, for which potent antimicrobial effects have been previously reported (9, 10). The wide band gap of TiO_2 (3.2 eV) (25) necessitates UV exposure for photocatalytic effects. While this may be a disadvantage from an application perspective, it allows particle-membrane interactions "in darkness" to be conveniently differentiated from oxidation effects, of importance for dissecting mechanistic aspects. As antimicrobial peptide, LL-37 (LLGDFFRKSKEKIGKEFKRIVQRIKDFLRNLVPRTES) was chosen, as this is a widely used benchmark peptide, displaying potent antimicrobial and anti-inflammatory effects (26). This peptide was also used in our previous study of oxidative degradation of bacterial lipid membranes by AMP-coated TiO_2 NPs (22), thus enabling comparison of results for two key components in bacterial cell walls, i.e., phospholipids and lipopolysaccharides. Complementing this, studies were performed for polyarginine homopolypeptide, allowing effects of positive charges alone for the effects above to be elucidated. Regarding lipopolysaccharides, studies were performed for both "rough" and "smooth" forms of Gram-negative LPS ("smooth" characterized by longer polysaccharide moieties and a lower

negative charge density than “rough” (27, 28)), as well as for Gram-positive LTA (having a smaller hydrophobic acyl moiety than Gram-negative LPS (29)).

For these systems, we employed neutron reflectometry (NR) and quartz crystal balance with dissipation (QCM-d) for studies of particle binding and UV-induced degradation, while fluorescence spectroscopy was used for monitoring ROS generation, and dynamic light scattering/ζ-potential measurements for studies of nanoparticle properties. Furthermore, small-angle X-ray scattering (SAXS), light scattering, and cryogenic transmission electron microscopy (cryoTEM) were used to investigate lipopolysaccharide and lipopolysaccharide-nanoparticle co-aggregate structure in absence and presence of nanoparticles and/or UV exposure. Monitoring how such physicochemical properties translate into anti-inflammatory effects of bare and peptide-coated TiO_2 nanoparticles, LPS/LTA-induced cell activation and toxicity were investigated for human monocytes. Considering the systemic nature of inflammation, the study was performed at physiologic pH 7.4 (30-32).

Materials and Methods

Materials. TiO_2 NPs (anatase, 4-8 nm) were supplied by PlasmaChem GmHb (Berlin, Germany). TiO_2 NPs were previously characterized by cryo-TEM and Small-Angle X-ray scattering (SAXS) (22). To obtain information on the size of primary particle size (i.e., not aggregated), such measurements were conducted at pH 3.4, where TiO_2 NPs are dispersed as single particles. SAXS results were fitted to a log-normal distribution, yielding an average nanoparticle size of 3 ± 1 nm, while cryo-TEM revealed a population of polydisperse particles with an average diameter of 2 ± 1 nm, and sizes from 0 to 10 nm. LL-37 (LLGDFFRKSKEKIGKEFKRIVQRIKDFLRNLVPRTES; >95%) was from Thermo Fisher Scientific (US). Polyarginine (Mw 5-15 kDa), whileoctadecyltrichlorosilane (OTS), smooth LPS from *Escherichia coli* (*E. coli*) O111:B4 (L2630), rough LPS from *E. coli* F583 (L6893), lipid A from *E. coli* F583 (L5399), and LTA from *S. aureus* (L2515) were all form Sigma Aldrich. Palmitoyloleoylphosphocholine (POPC), palmitoylarachidonoyl phosphocholine (PAPC), and palmitoyloleoylphosphoglycerol) (POPG) were from Avanti Polar Lipids (Alabaster, US). C_{11}-BODIPY 581/591 was from Molecular Probes/Thermo Fisher Scientific (US). Ultra-pure MilliQ water (MQ, 18.2 MΩ · cm) and D_2O (99% deuterated, Sigma Aldrich) were used to prepare all solutions. All other chemicals used were of analytical grade.

Liposome preparation. Liposomes were prepared as described previously (24). Briefly, 10 mg/mL lipid stocks in chloroform were mixed in dark glass vials to 50/25/25 (mol/mol) POPC/PAPC/POPG ('+PG'). The samples were then dried under N_2 and then kept for 2 h under vacuum. The resulting films were hydrated in 10 mM Tris, pH 7.4, to a concentration of 1 mg/mL. The dispersion was bath sonicated for 8 cycles, each consisting of 1 minute of sonication and 30 seconds of vortexing at 24°C, to obtain multilamellar vesicles (MLVs). These were then extruded 30 times through polycarbonate filters (Ø 100 nm, LipoFast miniextruder (Avestin, Ottawa, Canada)) to obtain large unilamellar vesicles (LUVs) for ROS studies.

Preparation of NPs-LPS and NPs-LTA mixtures. Mixed NPs-LPS or NPs-LTA samples were prepared 1:1 (wt) by dropwise addition of 25 µL of LPS or LTA (4,000 ppm (i.e., 4 mg/mL) in 10 mM Tris, pH 7.4) to 975 µL of either bare or peptide-coated TiO_2 (100 ppm (0.1 mg/mL) in 10 mM Tris, pH 7.4,), followed by vigorous vortexing. Samples were subsequently used for cryoTEM, SAXS, DLS, and ζ-potential studies.

Size and ζ-potential measurements. Dynamic and electrophoretic light scattering (DLS and ELS; 173° scattering angle) were performed using a Zetasizer Nano ZSP (Malvern Pananalytical Ltd., Malvern, UK) to obtain average particles sizes and ζ-potentials. Measurements were performed in triplicate at 25°C using automatic attenuation.

C_{11}-BODIPY 581/591 oxidation assay. Oxidation assay was performed as described before (33-35). In short, C_{11}-BODIPY 581/591 was incorporated into +PG vesicles. For this, 0.5 mol% of the dye was added to the organic solution prior to lipid film drying under Ar atmosphere. After hydration and extrusion, 0.5 mg/mL LUVs were subjected to *in situ* UV exposure (Spectroline ENF-260C, 254 nm; 3 mW/cm^2, sample-lamp distance ~6 cm) in the presence or absence of bare or coated TiO_2 NPs (100 ppm). Fluorescence spectra (λ_{ex} = 485 nm; λ_{em} = 500-700 nm) were acquired using a Cary Eclipse fluorescence spectrophotometer with Xe pulse lamp (Agilent Technologies, USA), and oxidation levels quantified by the shift of probe emission from red (λ_{max} = 594 nm) to green (λ_{max} = 520 nm) during the first 5-10 minutes. Experiments were also performed in the presence of ROS scavengers, i.e., D-mannitol ($^{\bullet}$OH scavenger (36)) and SOD ($^{\bullet}O_2^-$ scavenger (37)), to pinpoint effects of different ROS on lipid oxidation. All measurements were performed in duplicate at 37°C.

Cryogenic transmission electron microscopy (cryo-TEM). Cryo-TEM experiments were performed using a JEM-2200FS transmission electron microscope (JEOL) at the National Center for High Resolution Electron Microscopy (nCHREM), Lund University. A bottom-mounted TemCam-F416 camera (TVIPS) was employed to record zero-loss images at an acceleration voltage of 200 kV. Four µL droplets of the samples were deposited on a lacey formvar carbon coated grid (Ted Pella) and blotted with filter paper to remove excess fluid. The grid was then plunged into liquid ethane (-180 °C), to ensure rapid vitrification. Specimens were then stored in liquid nitrogen (-196 °C) and transferred into the microscope right before image acquisition, employing a cryo transfer tomography holder (Fischione Model 2550). Image analysis was performed with the software ImageJ (38, 39).

Synchrotron Small-angle X-ray scattering (SAXS). Structural features of LPS and LTA, as well as their changes under UV treatment in the absence and presence of bare and peptide-coated TiO_2 NPs, were studied through Synchrotron SAXS experiments at the BioSAXS beamline BM29 (ESRF, Grenoble, France) (40). An X-ray monochromatic radiation with energy=12.46 keV was employed to collect the scattering profiles in the $0.05 \leq q \leq 5$ nm^{-1} q (magnitude of the scattering vector) range, with a Pilatus3 2M detector operating in vacuum and at fixed sample–to-detector distance of 2.849 m. Bare TiO_2 NPs and mixed NPs-LPS or NPs-LTA samples (before and after UV illumination) in 10 mM Tris buffer, pH 7.4, were pipetted from Eppendorf PCR tube strips by an automatic sample changer and transferred in a quartz glass capillary (1 mm diameter) for scattering acquisition. Thirty 2D-images of 0.5 s exposure each were collected for each sample and for the buffer. Data were automatically processed to provide buffer-subtracted averaged scattering profiles (41). All measurements were performed at 25 °C.

Quartz crystal microbalance with dissipation monitoring (QCM-d). QCM-d measurements were performed using a QSense Analyzer equipped with both standard and UV-transparent sapphire window modules (Biolin Scientific, Sweden). LPS and LTA layers were formed on hydrophobic polystyrene-coated surfaces (QSense QSX 305 PS-Hydrophobic Polystyrene, 4.95 ± 0.05 MHz, 17.7 ng/cm^2 mass sensitivity; Surface roughness < 1 nm Root Mean Square (RMS)). The contact angle of water at such polystyrene surface was ~92° at room temperature, as previously determined (42, 43). Cells and tubings were thoroughly cleaned with 2% Hellmanex solution and multiple MQ rinses, combined with bath sonication, then rinsed in pure ethanol and dried under N_2. Polystyrene-coated surfaces were then mounted into measurement chambers. Dispersions of smooth LPS, Lipid A and

LTA were prepared in 10 mM Tris, 150 mM NaCl, pH 7.4, at a 400 ppm, while a higher concentration (1,000ppm) was needed for rough LPS to form a dense monolayer. Triethylamine (4% w/w) was added to the lipid A dispersion to ensure solubility in the aqueous buffer (44). Samples were tip-sonicated for 5 minutes (UP50H, Hielscher Ultrasonics GmbH, Germany (50 W, 30 kHz) used in an intermittent-pulse mode (5 s), at 100% amplitude) and subsequently injected using a peristaltic pump. A liquid flow of 0.1 mL/min was employed throughout the experiments. Sample deposition and layer formation were monitored from frequency shifts (ΔF) and dissipation changes (ΔD). This was followed by rinsing with 10 mM Tris, 150 mM NaCl, pH 7.4, to remove excess sample. Subsequently, bare or peptide-coated TiO_2 NPs (100 ppm in 10 mM Tris, 150 mM NaCl, pH 7.4) were flushed into the measurement chamber, followed by exposure to UV light for 2 h (Spectroline lamp ENF-260C, 6 W, 254 nm; 3 mW/cm^2, placed at ~ 2 cm from the QCM-d cell). Measurements were performed at 25°C at least in duplicate.

Neutron reflectometry (NR). Structural features of supported smooth LPS layers before, during, and after exposure to UV in the presence of LL-37-coated TiO_2 NPs were characterized by NR, employing the D17 vertical reflectometer (Institut Laue-Langevin, Grenoble, France) (45, 46). The whole Q-region of interest (~0.01 to 0.3 Å^{-1}) was covered using two incident angles (0.8° and 3.0°). NR experiments on supported smooth LPS layers interacting with bare TiO_2 NPs were performed on the OffSpec reflectometer (ISIS Pulsed Neutron and Muon Source, Rutherford Appleton Laboratory, Harwell, UK (47)). For these experiments, three incident angles (0.3°, 1.0° and 2.3°) were used to cover the Q-region from ≈0.01 to 0.35 Å^{-1}, achieving an instrumental resolution of 0.04 (4%) dq/q. Solid-liquid flow cells, with a top plate modified with a 30 mm diameter circular opening, were used in combination with UV-transparent quartz blocks (80×50×15 mm, 1 face polished, RMS < 4.5 Å, PI-KEM Ltd., Tamworth, UK) to allow *in situ* UV irradiation. The blocks were cleaned by bath-sonication for 30 min in chloroform, followed by acetone (30 min), ethanol (30 min), MQ (30 min) and ethanol (30 min). Then, they were dried under N_2, followed by 30 min of UV-ozone treatment (UV/Ozone ProCleaner, BioForce Nanosciences, USA). After that, they were dried in oven (100° C) for 10 min and transferred in a 1 mM octadecyltrichlorosilane (OTS) solution in toluene containing, followed by 1 h of incubation in a glovebox under N_2 flow (48, 49). This procedure allowed to form a hydrophobic OTS monolayer onto the block surface, characterized by ~ 100° contact water contact angle (50, 51). Blocks were finally rinsed with toluene and ethanol, dried under N_2 flow and mounted into solid-liquid flow cells. HPLC tubing, PEEK troughs, and O-rings were immersed in a 2%

Hellmanex (Hellma Analytics, UK) solution and cleaned by bath-sonication. Then, they were then thoroughly rinsed and sonicated in MQ. A circulating water bath was used during the measurements to keep the sample cells at 25°C.

OTS-coated surfaces were characterized in three contrasts, 10 mM Tris, 150 mM NaCl, pH 7.4 in MQ (h-Tris), D_2O (d-Tris), and 68.6/31.4 % v/v D_2O/MQ to match the scattering length density (SLD) of the quartz substrate (qm-Tris). Then, cells were rinsed with h-Tris containing $CaCl_2$ 4 mM (10 min, 2mL/min), followed by rinsing with h-Tris (10 min, 2mL/min). Twenty mL of smooth LPS in h-Tris (1,000ppm) were manually injected immediately after tip-sonication (5 min, UP50H, Hielscher Ultrasonics GmbH, Germany (50 W, 30 kHz) used in an intermittent-pulse mode (5 s), at 100% amplitude), and allowed to deposit for 30 minutes, after which excess material was rinsed off with 10 mL h-Tris at 1 mL/min. The layers thus formed were characterized in h-, qm-, and d-Tris. Contrasts were changed by pumping 20 mL of the desired buffer at 1 mL/min. After that, either 15 mL of bare or LL-37-coated TiO_2 NPs (100 ppm in h-Tris) were injected manually, followed by 10 min incubation. H-Tris was subsequently flushed to remove NP excess and samples characterized in h-, qm-, and d-Tris. The systems were then subjected to *in situ* UV irradiation (Spectroline lamp ENF-260C, 6 W, 254 nm; 3 mW/cm^2, placed at ~2 cm from the NR cell) for 2 h. Immediately after UV exposure, samples were rinsed with 20 mL of d-Tris (1 mL/min) and the whole Q-range measured in the three contrasts. The reflected intensity was measured as a function of the momentum transfer $q_z = (4\pi\backslash\lambda)\cdot\sin(\vartheta)$, with λ the wavelength and ϑ the incident angle. Quantitative information about the density profile of the sample normal to the interface was obtained by fitting the experimental data. Experimental NR profiles were fitted by using the Genetic Optimization method available on the analysis package Motofit within software IGOR Pro (52, 53). A series of parallel layers were used to model the interfacial structure, each of these described by a set of physical parameters, including thickness, roughness, hydration, and scattering length density (SLD). The best fits of these parameters were then converted into SLD profiles, showing the density distribution in the direction perpendicular to the reflecting interface. Monte Carlo error analysis allowing refitting data 200 times was employed to minimize the uncertainty associated with data fitting (54).

Cell experiments. Human THP1 monocytes (THP1-Xblue™-CD14 reporter cells, InvivoGen, France) were cultured according to manufacturer instructions, and effects of NPs on lipopolysaccharide-induced NF-κB activation monitored. To this purpose, 100 ppm bare or LL-37-coated TiO_2 NPs were mixed with 100 ppm smooth LPS or rough LPS, or 5,000 ppm LTA in 10 mM

Tris, pH 7.4 in quartz cuvettes. Samples were then incubated for 2 h at room temperature, either in darkness or under UV illumination (Spectroline ENF-260C, 254 nm; 3 mW/cm^2) at a sample-light distance of 6 cm. Cells (1x10^6 cells/mL) were incubated with these samples after dilution in 10 mM Tris to a final concentration of 0.1 ppm for LPS or 5 ppm for LTA. Solutions with or without LPS or LTA were used as positive and negative controls, respectively. After incubation (18−20 h) in 5% CO_2 at 37 °C, NF-κB activation was determined by incubating cell culture supernatants with the detection substrate (Quanti-Blue, InvivoGen, France) for 1−2 h, followed by quantification at 600 nm (n = 3). To investigate cell toxicity effects, a lactic acid dehydrogenase (LDH) assay was employed. For this, THP1 cells were incubated as above for 18−20 h and LDH release measured using a lactate dehydrogenase assay kit (Invitrogen™ CyQUANT™ LDH Cytotoxicity Assay, Thermo Fisher Scientific), according to the manufacturer's instructions.

Statistical Analysis. All data are reported as means +/- Standard Error of Mean (SEM). For all the experiments (except for NR and cryo-TEM experiements), measurements were conducted in at least triplicate. For NR, errors associated with the structural parameters of the lipopolysaccharides layers were obtained through a Monte Carlo error analysis (54) within the Motofit software embedded in the IGOR Pro analysis package (52, 53). This allowed refitting experimental NR profiles 200 times, minimizing the uncertainty associated with data fitting. For cryo-TEM, a minimum number of 20 image were acquired for each sample to achieve statistically significant morphological and structural information.

Results

Peptide coating of TiO_2 NPs

TiO_2 NPs have previously been reported to have an isoelectric point (IEP) at pH 6-6.5 (55,56). In line with this, the TiO_2 NPs employed in the present study displayed a positive ζ-potential at pH 3.4 and 5.4, a weak negative potential at pH 7.4, and a strongly negative potential at pH 9.4 (**Figure 1A**). Mirroring this, TiO_2 NPs displayed pronounced aggregation at pH 5.4 and 7.4, but much less so at pH 3.4 and 9.4. On loading TiO_2 nanoparticles with cationic LL-37 at pH 7.4, a concentration-dependent increase in positive ζ-potential was observed (**Figure 1B**). At saturation binding, a net positive ζ-potential of +22±3 mV was observed for TiO_2 NPs coated with LL-37. As a result of this, colloidal stability increased significantly at high peptide loading, as seen from the decrease in the

effective particle size. Based on these results, full peptide loading was inferred to occur at the peptide concentration of 50 µM, beyond which only marginal effects on ζ-potential and particle size were observed. Below, TiO_2 NPs loaded at this peptide concentration are referred to as LL-37-TiO_2.

Next, we investigated if peptide loading influenced ROS generation. Since electrons and holes generated during illumination need to react with water and dissolved oxygen for ROS formation, it is essential for the photocatalytic effects of coated TiO_2 NPs that the coatings allow such reactions to occur. As shown in **Figure 1C**, LL-37 coating did not markedly suppress ROS generation (see also **Figure S1A** for corresponding oxidation kinetics). Furthermore, quenching results showed both $^{\bullet}OH$ and $^{\bullet}O_2^-$ to be formed on UV illumination for bare TiO_2 and LL-37-TiO_2 alike (**Figure 1C**; see also Figure **S1B-C** for corresponding oxidation kinetics). As $^{\bullet}OH$ and $^{\bullet}O_2^-$ are highly reactive radicals, able to degrade proteins and polypeptides through oxidation (57), there is a risk that the LL-37 coating formed on TiO_2 NPs degrades upon UV illumination. Addressing this, we investigated the ζ-potential of the LL-37-coated TiO_2 nanoparticles after different durations of UV illumination. While a minor decrease in the positive ζ-potential was found, indicating some peptide degradation and/or oxidation, LL-37-coated TiO_2 NPs remained positively charged also after 2 h of UV exposure (**Figure 1D**). Thus, irrespective of degradation, most of peptide (including any fragments formed during UV illumination) remained bound at the nanoparticle surface, where they provided an electrostatic driving force for binding to negatively charged lipopolysaccharides.

Nanoparticle interactions with Gram-negative LPS and Gram-positive LTA in solution

Next, we investigated co-aggregates formed by bare or peptide-coated TiO_2 NPs with anionic LPS or LTA (see **Figure S2** for hydrodynamic size and ζ-potential of LPS and LTA in the absence of NPs). Mixing 100 ppm of LL-37-TiO_2 with 100 ppm smooth LPS resulted in very large (≈1,000 nm) co-aggregates of near-neutral surface charge. Similar-sized co-aggregates of larger negative surface charge were observed for rough LPS and LTA (**Figure S3**). A similar behavior was observed for LPS and LTA mixed with bare TiO_2 NPs, although aggregation by the TiO_2 NPs alone at this pH obscures effects of lipopolysaccharide-NP co-aggregation (**Figure 1A**). No major variations in aggregates size and ζ-potential were observed after 2 h of UV illumination for any of the samples.

To obtain further information on the structure of co-aggregates formed by LPS or LTA with peptide-coated TiO_2 NPs, we investigated these by cryoTEM. As shown in **Figure 2**, both smooth and rough

LPS, as well as LTA, form thread-like structures at pH 7.4, in line with previous findings (58-60). (Note, however, that lipopolysaccharide aggregates are not equilibrium structures, thus their self-assembly structure depend on preparation method. For example, smaller and less thread-like structures can be obtained after repeated extrusion or tip-sonication (61-63)). On addition of LL-37-TiO_2 NPs (**Figure 2**), the latter distributed homogeneously over the fiber structures of both smooth and rough LPS, as well as LTA, and triggered formation of dense co-aggregates. Furthermore, scattered multilamellar structures were observed in presence of LL-37-TiO_2, similar to those observed previously in the presence of free peptide (64). On UV illumination, the co-aggregates packed more densely (**Figure 3**), likely a result of degradation of some of the LPS chains, relaxing the kinetic constraints for dense packing. In line with this, free LPS fragments were observed on illumination, most clearly seen outside co-aggregates formed between LL-37-TiO_2 NPs and rough LPS (**Figure 2**). These findings are in line with the dynamic light scattering results discussed above. To more conclusively elucidate if degradation caused formation of ordered structures, SAXS was employed. However, no ordered structures were observed for either LPS or LTA (**Figure S4**), possibly due to their long hydrophilic and negatively charged polysaccharide chains (27-29), and/or by the signal from these being masked by the broad NP signal.

Nanoparticle interactions with surface-bound LPS, lipid A, and LTA

Mirroring the "end-on" orientation of LPS in the outer membrane of Gram-negative bacteria, we next investigated smooth and rough LPS bound to hydrophobic polystyrene substrates through their hydrophobic lipid A moiety, employing QCM-d. Also lipid A alone was investigated. While compositions and procedures had to be optimized for the different systems, conditions were found at which all three systems formed well-defined adsorbed layers (**Figure 4**). On addition of bare TiO_2 NPs (carrying a weak negative ζ-potential; **Figure 1A**), very little binding to the negatively charged LPS or lipid A was observed (**Figure S5A** for results on binding and **Figure S6A** for corresponding kinetics; note, however, that NR shows that minor adsorption does in fact occur to these surfaces; cf below). In contrast, LL-37-coated TiO_2 NPs displayed pronounced initial binding to both smooth and rough LPS, as well as to lipid A, but then caused partial desorption of rough LPS and lipid A after initial binding (**Figure 5A** for results on binding and **Figure S7A** for corresponding kinetics). For smooth LPS, no partial desorption was observed, likely due to its longer carbohydrate chains precluding close contact between the peptide-coated nanoparticles and its lipid A moiety (see also discussion of NR results below).

On UV exposure after LL-37-TiO_2 NPs binding, desorption triggered by oxidative degradation was observed for both smooth and rough LPS, as well as for lipid A (**Figure 5B** and **S7B**). Similar results were observed for bare TiO_2 (**Figure S5B** for results on desorption and **Figure S6B** for corresponding kinetics). For LL-37-TiO_2, NP binding to LTA was comparable to that for rough LPS (**Figures 5A** and **S7A**). Also on UV exposure, LTA behaved similarly to LPS (**Figures 5B** and **S7B**).

Structural aspects of LPS degradation

To obtain more detailed information on structural features of UV-induced LPS degradation, NR was employed for LL-37-TiO_2 interacting with smooth LPS. The effect of bare TiO_2 was also investigated for comparison. Experiments were performed in 10 mM h- and qm-Tris, pH 7.4, containing 150 mM NaCl. For this, quartz blocks were pre-coated with a homogeneous hydrophobic layer of OTS (48,63) as pre-coating with polystyrene (used in the QCM-d experiments) were deemed incompatible with the high smoothness requirements of NR experiments. OTS layer was characterized in three contrasts (**Figure S8**). The structural parameters of this layer, obtained from NR fits (**Table S1**), were consistent with previous literature (48,63). Smooth LPS was then manually injected into the measurement chamber and the reflectivity changes following the LPS layer formation were monitored. NR profiles acquired in h-, qm- and d-Tris were fitted simultaneously to a 3-layer model (**Scheme S1**). NR profiles, for smooth LPS interacting with either bare or LL-37-TiO_2 NPs, before and after UV illumination, together with best curve fits and corresponding SLDs, are reported in **Figure S9**. Key structural data determined through fitting are plotted in **Figures 6** and listed in **Tables S2** (bare TiO_2 NPs) and **S3** (LL-37-TiO_2 NPs). Prior UV illumination, the incubation with bare TiO_2 NPs did not induce significant structural modification in any of the LPS domains, i.e. lipid A, core oligosaccharide, and O-antigen chain. In contrast, the addition of LL-37-TiO_2 NPs provoked a substantial decrease in thickness of the outer O-antigen chains layer, from 124 ± 24 Å to 40 ± 7 Å. UV illumination induced a further decrease in the thickness of O-antigen chains (to 9 ± 1 Å) and hydration (from 94 ± 1 % to 59 ± 8 %), indicating an almost complete removal of the outer O-antigen layer. In contrast, only a relatively minor thickness reduction of the O-antigen layer was detected on UV illumination in the presence of bare TiO_2 NPs, i.e., from 106 ± 12 Å to 84 ± 17 Å, with negligible hydration changes. For both bare and LL-37-coated TiO_2 NPs, the internal layers of OTS/lipid A and core oligosaccharides were largely unaffected by UV illumination.

Anti-inflammatory effects and cell toxicity

To investigate the biological relevance of the results obtained in the model lipopolysaccharide systems, we next investigated the capacity of the peptide-coated NPs to suppress activation of human monocytes by LPS and LTA, monitored as a decrease in LPS/LTA-induced NF-κB levels. As shown in **Figure 7A**, LL-37-TiO_2 NPs suppressed NF-κB for both smooth and rough LPS, as well as LTA, even in the absence of UV illumination. In contrast, minor effects were only observed for rough LPS in the case of bare TiO_2 NPs. On UV illumination, a further reduction in NF-κB was observed for smooth LPS, whereas bare TiO_2 NPs did not display any such effect. These findings are in line with the results obtained for the model systems showing: (i) co-aggregate formation and resulting lipopolysaccharide confinement for peptide-coated TiO_2 NPs, and (ii) UV-induced lipopolysaccharide degradation. While LL-37-TiO_2 NPs thus present boosted anti-inflammatory effects compared to bare TiO_2 NPs, cell toxicity remained low, at the level for bare TiO_2 NPs and lower than that for the negative control (**Figure 7B**).

Discussion

Cationic surface modifications of NPs have been widely found to promote their antimicrobial activities (3). Such effects are often ascribed to increased binding to negatively charged bacterial membranes. In addition, however, cationic surface modifications of nanoparticles have been frequently reported to display toxicity against human cells (3, 65, 66). Since conventional surface modifications to enhance antimicrobial effects and reduce toxicity of nanomaterials therefore seem insufficient to reach selectivity between bacteria and human cells, novel approaches are needed. Surface coating by AMPs has been suggested as a way to effectively "target" these to bacteria (18-22). For example, Malekkhaiat Häffner et al. coated laponite and other nanoclays with LL-37 and found such peptide-coated particles to display potent antimicrobial effects at simultaneously low toxicity against human monocytes (67, 68). Conceptually related, Duong et al. reported that coating of polymer particles with GRR10W4 increased uptake into melanoma cells (rich in anionic phospholipids), resulting in enhanced anti-cancer effects at simultaneously low toxicity against non-malignant fibroblasts and keratinocytes (69).

For photocatalytic NPs, AMP coating is inherently more complicated considering requirements of simultaneous ROS generation and oxidative robustness of the peptide coating. It is therefore interesting to note that Lu et al. (70), Zhang et al. (1), and Chen et al. (72) all reported on advantageous

functional performance of peptide-coated photocatalytic nanomaterials as antimicrobials, although not addressing the mechanistic foundation for such effects. In an effort to do so, we recently investigated the interactions of TiO_2 NPs coated with LL-37 by NR in combination with a battery of physicochemical methods and biological assays. From this, it was found that: (i) AMP coating did not markedly suppress ROS generation, (ii) the peptide coating was quite stable against ROS degradation, allowing (iii) dramatically improved binding to bacteria-like lipid membranes compared to bare TiO_2 NPs. As a result, (iv) UV-induced membrane degradation was boosted for bacteria-like membranes, whereas human cell-like membranes remained unaffected (27).

In a couple of studies, photocatalytic NPs have been found to suppress inflammation caused by LPS (73, 74), although the mechanistic origin of such effects remain unresolved. There is also a potential complication of photocatalytic NPs that oxidative degradation may result in the release of bacterial debris, which may potentially trigger inflammation, at least until lipopolysaccharide degradation has progressed sufficiently to result in fragments small enough not to cause cell activation. In Gram-negative bacteria, LPS forms a dense outer barrier, which may act as a barrier for nanoparticles (75), preventing proximity between ROS species formed on illumination and the inner plasma membrane. Such effects may contribute to lower antimicrobial effects against Gram-negative reported for photocatalytic NPs (8, 76). In relation to this, it is also relevant to consider the relative susceptibility of bacterial membrane components to photocatalytic degradation, i.e., phospholipids, bacterial lipopolysaccharides, and peptidoglycan. Addressing this, Kiwi et al. investigated TiO_2-mediated photocatalytic oxidation of *E. coli* bacteria, as well as of phosphatidylethanolcholine (PE), LPS, and peptidoglycan (PGN). PGN was found to be more resistant to photocatalytic degradation than both LPS and PE (77). Similarly, Liu et al. reported that while photocatalytic action by TiO_2 NPs was able to damage the outer bacterial membrane of *E. coli* bacteria, it was not able to destroy the peptidoglycan underneath, again demonstrating peptidoglycan to be more resilient to oxidative disintegration than phospholipids and LPS (78).

Regarding LPS degradation, Engel et al. investigated photocatalytic inactivation of *E. coli* bacteria by carbon nanotube heterostructures (79). Mutants with shorter polysaccharide chains were found to be more susceptible to photocatalytic degradation than those with long ones. As shown by the QCM-d results in the present investigation, LL-37-TiO_2 NPs are able to degrade both the lipid A, the core oligosaccharide, and the O-antigen moieties of LPS. Having said that, NR results show that when all

these moieties are present at the same time and in the proper orientation, as for s-LPS bound to hydrophobic surfaces through its lipid A moiety, LL-37-TiO_2 NPs preferentially degrade the outer O-antigen moiety. Another key finding of the present investigation is that of Gram-positive LTA displaying susceptibility to photocatalytic degradation comparable to that of Gram-negative LPS. However, LTA is located within the cross-linked peptidoglycan matrix of Gram-negative bacteria. Hence, even if LTA is photocatalytically degraded, it may be kinetically hindered to diffuse out of this matrix, particularly if the peptidoglycan matrix is resilient to photocatalytic degradation. As demonstrated by the findings of the present investigation, such kinetic arrest may be promoted by cationic peptide-coated TiO_2 NPs.

LTA, as well as smooth and rough LPS, co-aggregate strongly with LL-37-TiO_2 NPs. As such, these lipopolysaccharides are efficiently confined in co-aggregates, with very few lipopolysaccharide molecules in the solution surrounding the co-aggregates. As a result, lipopolysaccharide-mediated cell activation was suppressed, effectively providing the peptide-coated particles with anti-inflammatory properties also in the absence of UV illumination. On photocatalytic degradation, most LTA and LPS remain within increasingly densely packed co-aggregates, and only few fragments can be observed in the solution surrounding the lipopolysaccharide-NP co-aggregates. Importantly, there seems to be no intermediate degradation, during which lipopolysaccharide fragments are released to an extent triggering cell activation. In this context, it should also be noted that confinement of inflammatory response by co-aggregation has previously been observed for the antimicrobial peptide TCP96, which is released from thrombin in response to bacterial protease activity in wound fluids to allow localized inflammation but simultaneously suppressing delocalized inflammatory responses (80).

Taken together, the present study shows that peptide-coated TiO_2 nanoparticles may offer interesting opportunities for photocatalytic degradation of bacterial lipopolysaccharides at simultaneously low cell toxicity, with possibilities for confinement of infection and inflammation. Furthermore, the results provide some insight on the mechanism of such photocatalytic degradation, particularly regarding effects of: (i) lipopolysaccharide type (ii) LPS polysaccharide length, and (iii) the relative importance of polysaccharide and lipid A degradation.

However, numerous issues remain to be resolved regarding lipopolysaccharide degradation by

peptide-coated photocatalytic NPs. For example, while qualitatively similar effects were observed for AMP LL-37 and a similar-size polyarginine homopolymer regarding NP coating properties, and lipopolysaccharide binding, the results also indicate that photocatalytic degradation of peptide-coated NPs may be suppressed by overcharging the peptide (as for polyarginine) (**Figure S10**), presumably through electrostatic arrest preventing NP insertion into the lipopolysaccharide layers. Further studies are therefore needed to elucidate how peptide properties such as charge, hydrophobicity, and length, key for lipopolysaccharide interactions of free AMPs, translate into anti-inflammatory effects of the corresponding particle-bound AMP systems.

Conclusions

On coating TiO_2 NPs (IEP≈6.5) with the antimicrobial peptide LL-37 (IEP≈11.2), colloidal stability at physiological pH-range was strongly enhanced. Moreover, the peptide coating was stable over at least two hours of UV illumination and did not detrimentally affect ROS generation. As a result of the positive charge of the peptide-coated NPs, binding to anionic bacterial lipopolysaccharides was strongly promoted. The peptide-coated NPs distributed uniformly over the lipopolysaccharides and resulted in dense co-aggregates. On UV-induced degradation, packing constraints induced by chain-like LPS were relaxed, resulting in denser co-aggregates as well as in efficient capture of lipopolysaccharide fragments formed. Monitoring structural aspects of these processes, neutron reflectometry showed LPS degradation of LL-37-TiO_2 NPs to occur preferentially in its outer O-antigen region. Gram-positive LTA showed qualitatively similar effects as Gram-negative LPS regarding UV-induced degradation, co-aggregate densification, and absence of ordered structure formation. These effects were found be relevant to the ability of peptide-coated TiO_2 NPs to suppress inflammatory activation by bacterial lipopolysaccharides. In addition, the peptide-coated TiO_2 NPs displayed low toxicity against human monocytes, showing a potential of such NPs to effectively localize inflammatory responses at simultaneously low toxicity.

Ethics approval and consent to participate

Not applicable.

Consent for publication

All authors read and agree this version be published.

Availability of data and materials

No datasets were generated or analysed during the current study.

Competing interests

The authors have no competing interests as defined by BMC, or other interests that might be perceived to influence the results and/or discussion reported in this paper.

Funding

Neutron beamtimes were awarded by ILL (10.5291/ILL-DATA.9-13-1047) and ISIS (10.5286/ISIS.E.RB2310291). The research was funded by the Swedish Research Council (Grant number 2021-05498; MM and LC), the Independent Research Fund Denmark (Grant number 9040-00020B; MM and LC), as well as the LEO Foundation (Grant numbers LF15007 and LF-ST-21-500005; (MvP and MM).

Authors' contributions

L.C. and M.M. conceptualized the study and wrote the main manuscript text. L.C. performed most of the experiments and data analysis. S.M., M. WA S., F.S., R. G. D., S. B. and T.T. participated in Neutron Reflectometry measurements. G. D. participated in cryo-TEM imaging and data analysis. M VDP. supervised biological experiments. All authors reviewed the manuscript.

Acknowledgements

We thank ILL (Proposal number 9-13-1047) and ISIS Neutron and Muon Source (10.5286/ISIS.E.RB2310291) for access to neutron beam time and solid-liquid interface cells. The research was funded by the Swedish Research Council (Grant number 2021-05498; MM and LC), Independent Research Fund Denmark (Grant number 9040-00020B; MM and LC), as well as the LEO Foundation (Grant numbers LF15007 and LF-ST-21-500005; MvP and MM).

Authors' information

[1]Department of Physical Chemistry 1, Lund University, SE-22100 Lund, Sweden

[2]Institut Laue–Langevin, CS 20156, 38042 Grenoble Cedex 9, France
[3]Department of Pharmacy, University of Copenhagen, DK-2100 Copenhagen, Denmark
[4]LINXS Institute of Advanced Neutron and X-ray Science, Scheelevagen 19, 22370 Lund, Sweden
[5]ISIS Pulsed Neutron and Muon Source, Rutherford Appleton Laboratory, OX11 0QX, Harwell, UK.

Supporting Material

Calculated SLDs, summaries of structural data obtained from neutron reflectometry experiments, neutron reflectivity curves and best fits, data on oxidation kinetics, as well as ζ-potential, oxidation assay, synchrotron-SAXS, and cryoTEM results, are available as Supporting Information. This material also includes input parameters used for NR fits and structural parameters obtained from NR fits.

Present Addresses

Lucrezia Caselli: Department of Chemistry "Ugo Schiff", University of Florence and CSGI, Florence, Italy.

Guanqun Du: CAS Key Laboratory of Colloid, Interface and Chemical Thermodynamics, CAS Research/Education Center for Excellence in Molecular Sciences, Beijing National Laboratory for Molecular Science, Institute of Chemistry, Chinese Academy of Sciences, Beijing 100190, P. R. China.

Samantha Micciulla: Centre National de la Recherche Scientifique (CNRS), Saint-Martin-d'Hères, Auvergne-Rhône-Alpes, France.

Tanja Traini: Technical University of Munich, Munich, Germany.

Figures

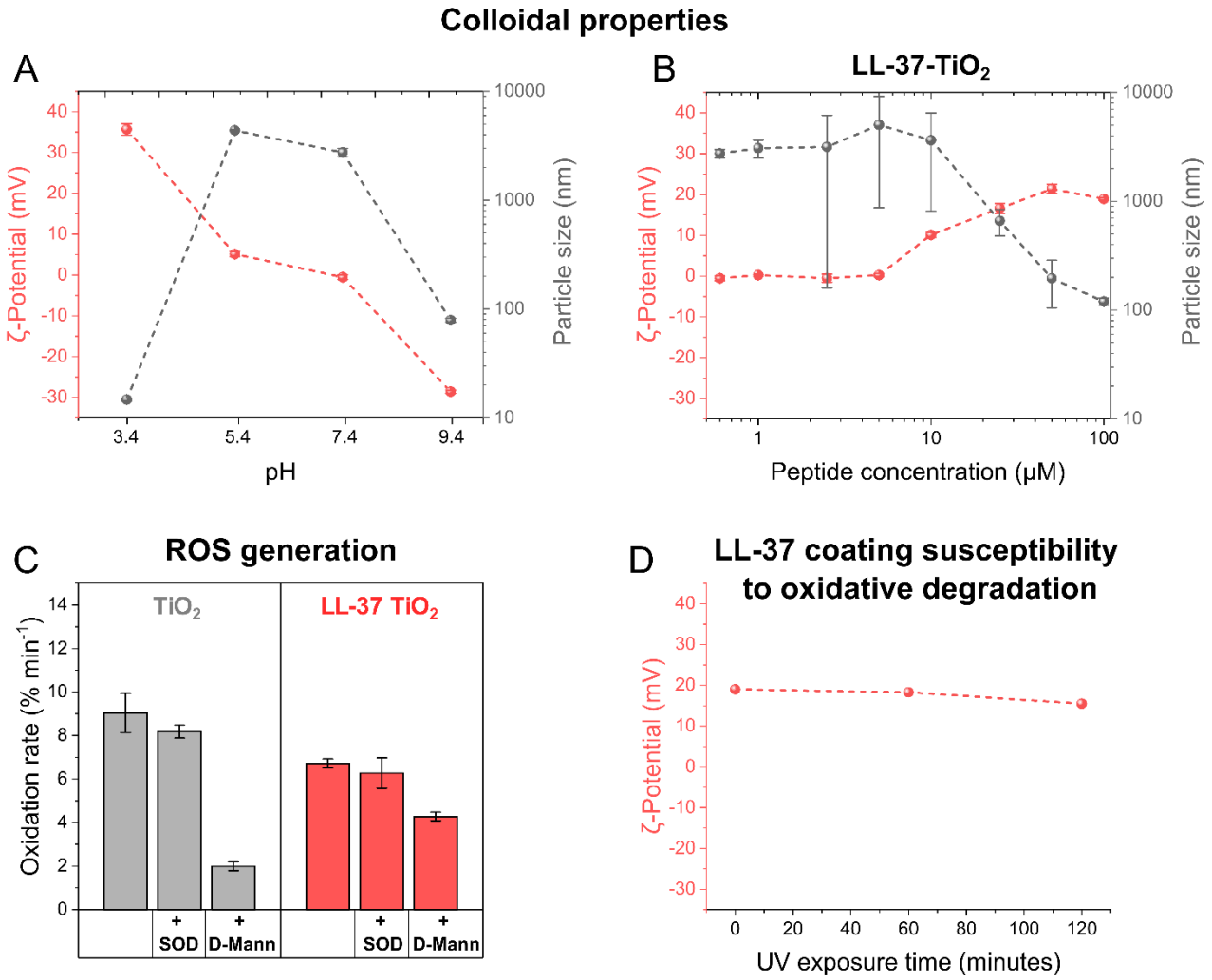

Figure 1. Characterization of LL-37-TiO_2 NPs. (A) ζ-potential and average particle size of bare TiO_2 NPs (100 ppm), in 10 mM acetate (pH 3.4 and 5.4) or 10 mM Tris (pH 7.4 and 9.4). (B) ζ-potential and average particle size of TiO_2 nanoparticles (100 ppm) loaded at varying concentrations of LL-37 in 10 mM Tris, pH 7.4. (n=3). (C) C_{11}-BODIPY oxidation rates for bare or LL-37-coated TiO_2 NPs on +PG LUVs subjected to *in situ* UV exposure in 10 mM Tris, pH 7.4. (n=3). Corresponding oxidation kinetics are shown in **Figure S1**. (D) ζ-potential of TiO_2 NPs coated with 50 μM LL-37 in 10 mM Tris, pH 7.4, before and after 1 or 2 h of UV illumination. Results are means +/- SEM of n=3 experiments.

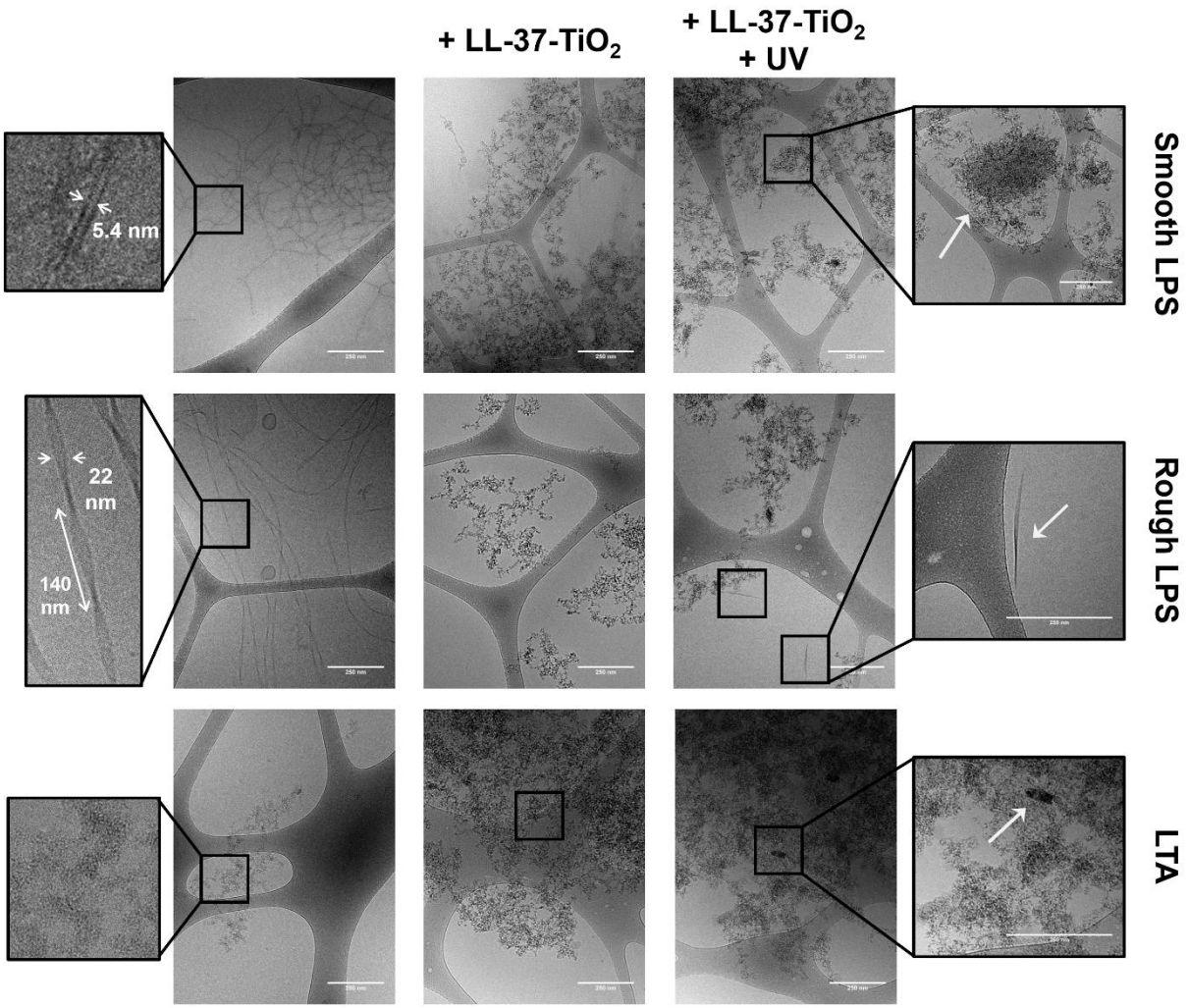

Figure 2. cryoTEM images for 100 ppm smooth LPS (top), rough LPS (middle), and LTA (bottom) in 10 mM Tris, pH 7.4 (left), as well as corresponding systems in the presence of 100 ppm of LL-37-TiO_2 NPs, either before (middle) and after (right) 2 h of UV illumination. The structural features of LPS and LTA (without LL-37-TiO_2 NPs) are highlighted in far-left insets, showing the formation of fibrillae with diameter of ~ 5 nm for smooth LPS, twisted ribbon-like structures of ~22 nm in thickness and ~140 nm characteristic node-to-node distance for rough LPS, and amorphous nanosized assemblies for LTA. Incubation with LL-37-TiO_2 NPs leads to aggregates of smooth LPS, rough LPS and LTA, homogeneously decorated with NPs. UV illumination results in increased packing density of such aggregates (**Figure 3**) and triggers the formation of characteristic structures (highlighted in the far-right insets), consisting of amorphous NP-decorated spherical assemblies (mostly observed in smooth LPS samples), free LPS fragments (mostly clearly seen in rough LPS samples) and multilamellar plate-like structure (present in both LPS and LTA samples).

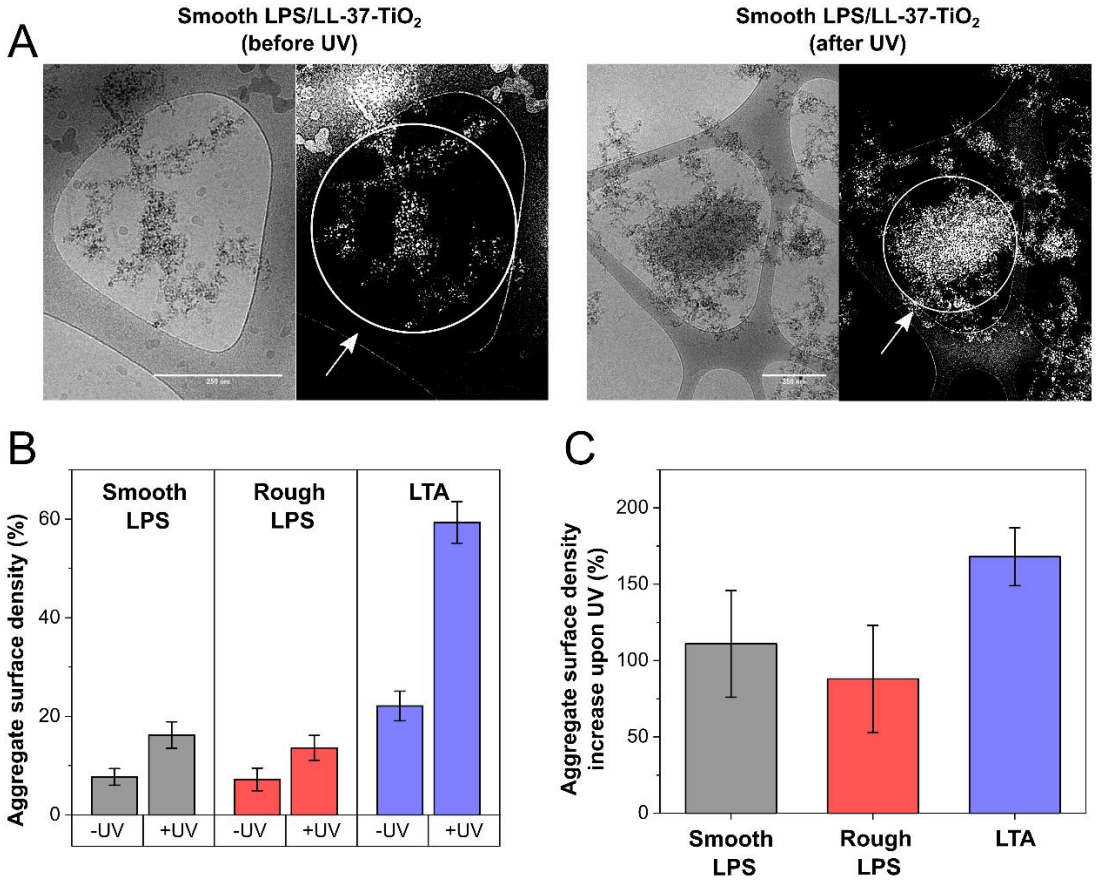

Figure 3. Quantification of the compactness of LL-37-TiO_2 co-aggregates with LPS and LTA, obtained through cryo-TEM image analysis with the software ImageJ (38, 39). The procedure adopted for image analysis is shown in (A) for representative images of smooth LPS/LL-37-TiO_2 co-aggregates, acquired before (left image) or after (right image) 2 h of UV illumination. Black and white mask images were obtained from original cryo-TEM images to allow precise mapping of the edges of LL-37-TiO_2/LPS or -LTA co-aggregates over the cryo-TEM grid. LL-37-TiO_2/LPS or -LTA aggregates were analyzed individually by selecting specific portions of the mask (e.g., areas highlighted in white in (A)). For aggregates smaller than the typical size of the holes in the cryo-TEM grid, the smallest circular areas fully enclosing the edges of single aggregates were selected. For aggregates exceeding this size, the largest circular areas enclosed within single grid holes were analyzed. The surface density of the aggregates (%) was then obtained over such selected portions as the ratio between the area occupied by the aggregate (in white) and the empty area (in black) and averaged over a large number of aggregates. Aggregates surface densities (%) for the different samples, before and after UV illumination, are reported in (B). Shown in (C) are also the percentage increases in the aggregates surface density (%) on UV exposure). Results reported in (B) and (C) are means +/- SEM of n≥20 aggregates per sample.

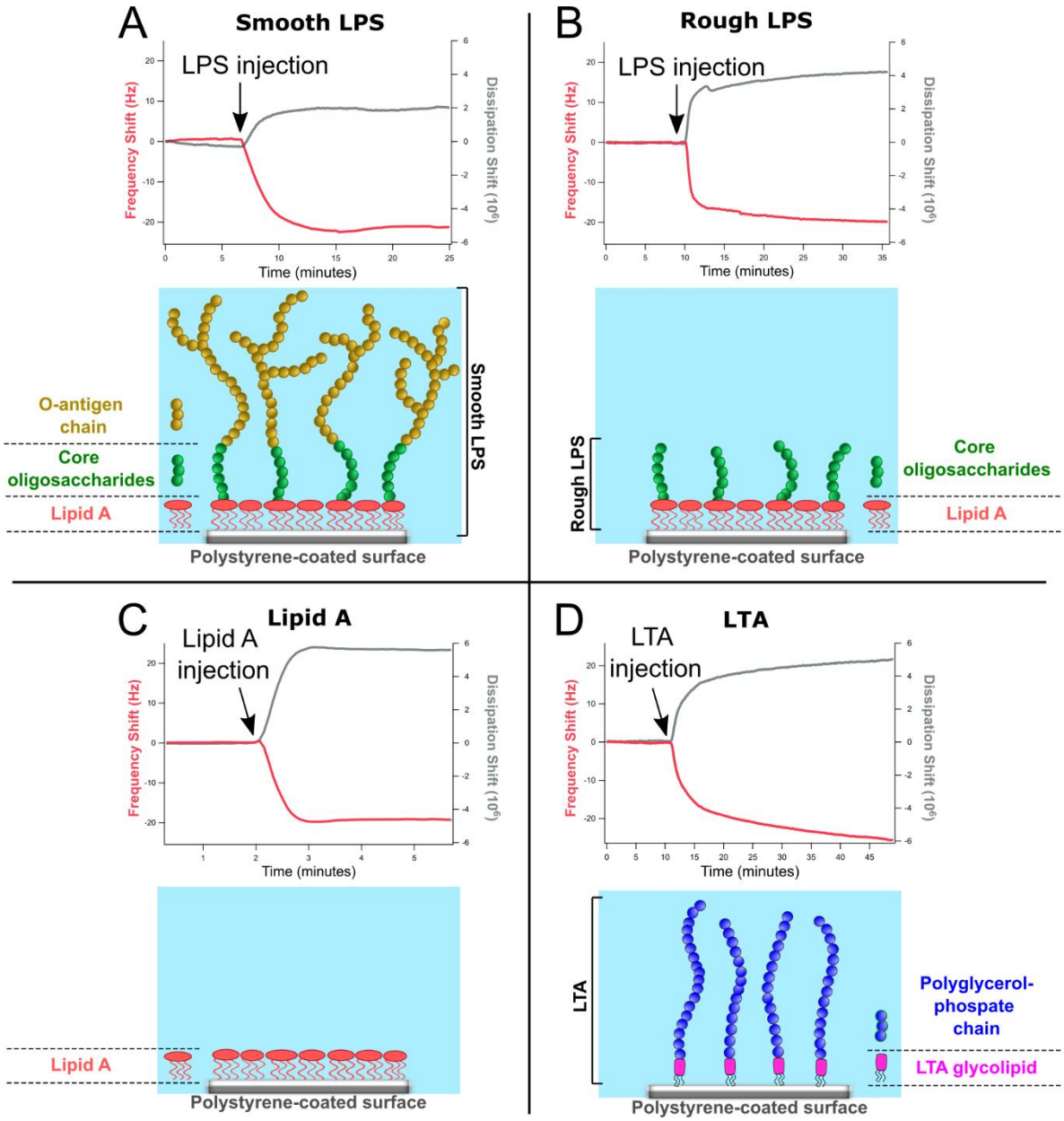

Figure 4. LPS and LTA layer formation. Representative QCM-d kinetics curves showing the 7th overtone of Frequency (ΔF) and Dissipation (ΔD) shifts associated to the formation of (A) smooth LPS layer by deposition on hydrophobic polystyrene from 400 ppm in 10 mM Tris, 150 mM NaCl, pH 7.4, (B) rough LPS layer on hydrophobic polystyrene from 1,000 ppm in 10 mM Tris, 150 mM NaCl, pH 7.4, (C) lipid A layer on hydrophobic polystyrene by deposition from 400 ppm in 10 mM Tris, 150 mM NaCl, pH 7.4, containing also triethylamine (4% w/w), and (D) LTA layer by deposition on hydrophobic polystyrene from 400 ppm in 10 mM Tris buffer, 150 mM NaCl, pH 7.4.

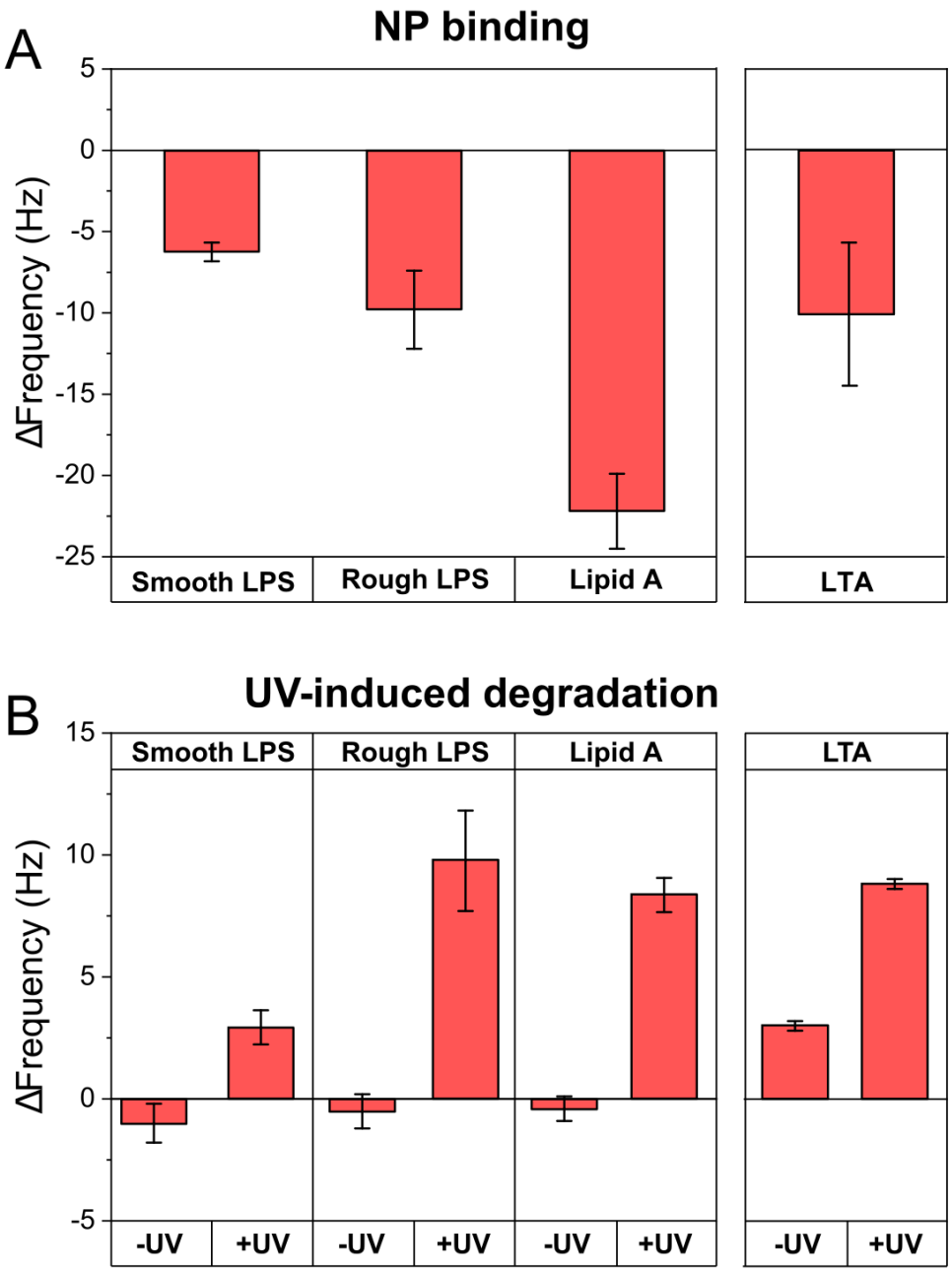

Figure 5. QCM-d results showing frequency shifts caused by (A) binding of 100 ppm LL-37-TiO_2 NPs to smooth LPS, rough LPS, lipid A and LTA; (B) effects of 2 h of *in situ* UV illumination for smooth LPS, rough LPS, lipid A and LTA interacting with 100 ppm LL-37-TiO_2. Results are shown for adsorption to hydrophobic polystyrene surfaces coated with smooth LPS, rough LPS, lipid A and LTA prepared as in **Figure 4**. ΔF=0 corresponds to the Frequency shift for the smooth LPS, rough LPS and Lipid A layers right before NP addition (A) or UV illumination (B). All measurements were performed in 10 mM Tris + NaCl 150 mM, pH 7.4. Representative QCM-d profiles for Figures (A) and (B) are shown in **Figure S7**, while corresponding results for bare TiO_2 NPs are shown in **Figures S5** and **S6**. Results are means +/- SEM of n=3 experiments.

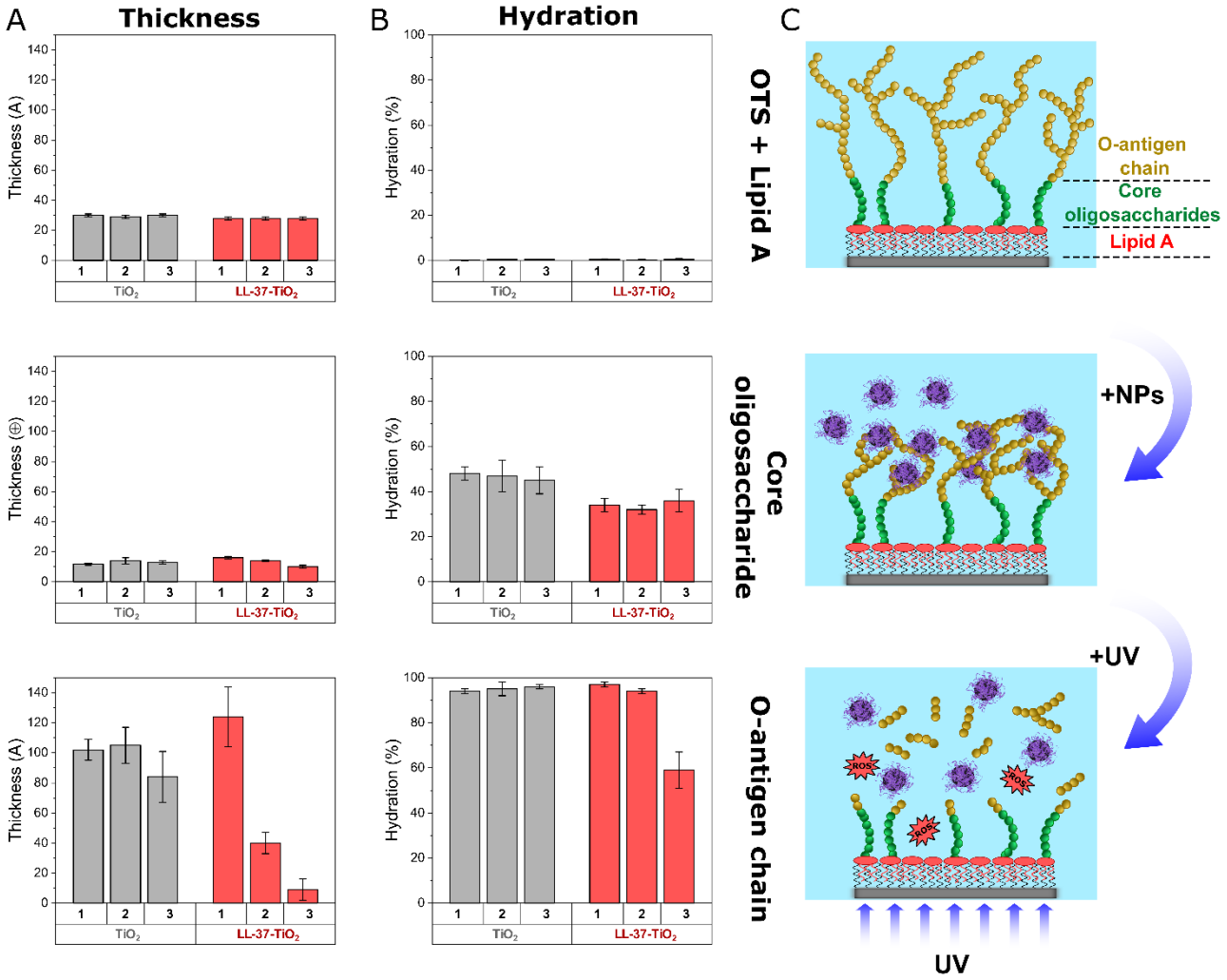

Figure 6. Structural effects on OTS + Lipid A (top), Core oligosaccharide (middle), and O-antigen chain (bottom) layers induced by bare and LL-37-coated TiO_2 NPs, in the absence and presence of UV illumination. Results were obtained from neutron reflectometry fits, calculating the physical parameters of the bilayers at different time points: (1) before NP incubation; (2) after NP incubation; (3) after 2 h of *in situ* UV exposure. Shown are changes in the thickness (A) and hydration (B) for the three different layers, as well as a schematic illustration (C) describing the main structural changes observed for the different LPS domains upon NPs interaction and UV illumination. Corresponding experimental curves, best curve fits and calculated SLD profiles, are shown in **Figure S13**, while **Figure S12** collects experimental curves, together with best curve fits and SLD profiles, for the neat OTS layer grafted before LPS deposition.

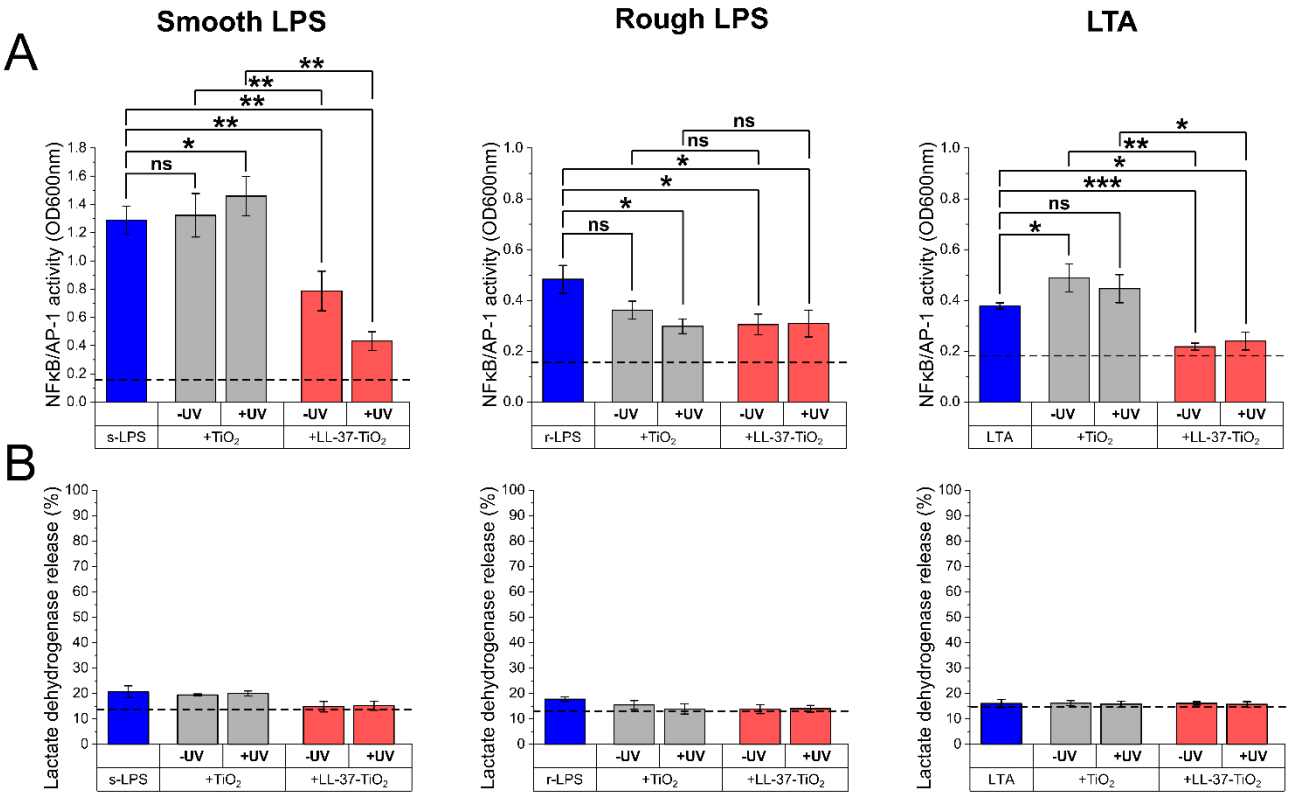

Figure 7. (A) NF-κB/AP-1 activation and (B) LDH release induced by smooth (left) and rough (middle) LPS, as well as LTA (right), in the absence and in the presence of bare TiO_2 or LL-37-TiO_2 NPs in 10 mM Tris, pH 7.4, either before or after 2 h of UV illumination, using THP1-XBlue-CD14 reporter monocytes. The dashed lines in the graphs represent the NF-κB/AP-1 activation or LDH release for the control sample, i.e., 10 mM Tris buffer, pH 7.4, in the absence of LPS, LTA and NPs. Results are mean +/- SEM of 3-7 experiments. Values are significantly different (* $p< 0.05$, ** $p<0.005$, and *** $p<0.0005$) as analyzed using a one-tailed paired t-test.

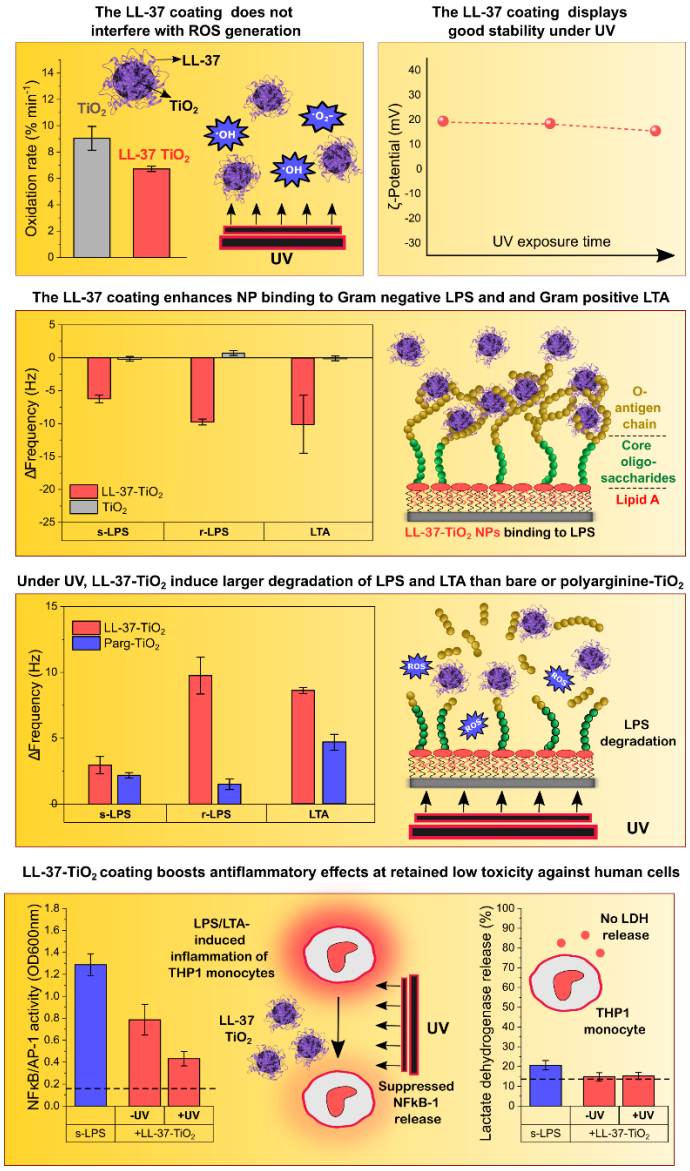

Figure 8. Schematic illustration of key findings of the study: LL-37 coatings on TiO_2 NPs did not detrimentally interfere with ROS generation and displayed good stability on UV exposure. As a result, binding of net cationic LL-37- TiO_2 NPs to anionic Gram-negative LPS, its lipid A moiety, and Gram-positive LTA was much higher than that to weakly charged bare TiO_2 NPs. Mirroring this, LL-37-TiO_2 displayed potent capturing and UV-induced degradation fragments from LPS and LTA. While qualitatively similar effects were observed for polyarginine-coated NPs, oxidative degradation for all systems was lower than that for LL-37-TiO_2 NPs, likely due to electrostatic arrest preventing the highly cationic polyarginine NPs from effectively incorporating into the lipopolysaccharide layers. Mirroring effects observed in model lipopolysaccharide systems, LL-37-coated TiO_2 NPs displayed boosted anti-inflammatory effects induced by both LPS and LTA at UV illumination, whereas toxicity against human monocytes remained low.

References

1. Zaman, S.B., Hussain, M.A., Nye, R., Mehta, V., Mamun, K.T., and Hossain, N. A review on antibiotic resistance: alarm bells are ringing. Cureus. 2017, 9, e1403, 1-9.

2. Blair, J.M.A., Webber, M.A., Baylay, A.J., Ogbolu, D.O., and Piddock, L.J.V. Molecular mechanisms

of antibiotic resistance. Nature Rev. Microbiol. 2015, 13, 51: 1-10.

3. Malekkhaiat Häffner, S., Malmsten, M. Membrane interactions and antimicrobial effects of inorganic nanoparticles. Adv. Colloid Interf. Sci. 2017, 248, 105-128.

4. Gupta, A., Mumtaz, S., Li, C.-H., Hussain, I., and Rotello, V. Combatting antibiotic-resistant bacteria using nanomaterials. Chem. Soc. Rev. 2019, 48, 415-427.

5. Lee, N.-Y., Ko, W.-C., and Hsueh, P.-H. Nanoparticles in the treatment of infections caused by multidrug-resistant organisms. Front. Pharmacol. 2019, 10, 1153:1-10.

6. Collin, F. Chemical basis of reactive oxygen species reactivity and involvement in neurodegenerative diseases. Int. J. Mol. Sci. 2019, 20, 2407: 1-17.

7. Parra-Ortiz, E., and Malmsten, M. Photocatalytic nanoparticles – from membrane interactions to antimicrobial and antiviral effects. Adv. Colloid Interface Sci. 2021, 102526: 1-19.

8. Yadav, H.M., Kim, J., Pawar, S.H. Developments in photocatalytic antibacterial activity of nano TiO2: a review. Korean J. Chem. Eng. 2016, 33, 1989-1998.

9. Sułek, A., Pucelik, B., Kuncewicz, J., Dubin, G., and Dabrowski, J.M. Sensitization of TiO2 by halogenated porphyrin derivatives for visible light biomedical and environmental photocatalysis. Catal. Today 2019, 335, 538-549.

10. Ahmed, F.Y., Aly, U.F., Abd El-Baky, R.M., and Waly, N.G.F.M. Comparative study of antibacterial effects of titanium dioxide nanoparticles alone and in combination with antibiotics and MDR Pseudomonas aeruginosa strains. Int. J. Nanomed. 2020, 15, 3393-3404.

11. Henriksen, J, Rowat, A.C., Brief, E., Hsueh, Y.W., Thewalt, J.L., Zuckermann, M.J., and J.H. Ipsen, J.H. Universal behavior of membranes with sterols. Biophys. J. 2006, 90, 1639-1649.

12. Haest, C.W., de Gier, J., den Kamp, J.A., Bartels, P., and van Deenen, L.L. Changes in permeability of Staphylococcus aureus and derived liposomes with varying lipid composition. Biochim. Biophys. Acta, 1972, 255, 720-733.

13. Epand, R.F., Savage, P.B., and Epand, R.M. Bacterial lipid composition and the antimicrobial efficacy of cationic steroid compounds (Ceragenins). Biochim. Biophys. Acta 2007, 1768, 2500-2509.

14. van Meer, G. Lipid traffic in animal cells. Annu. Rev. Cell Biol. 1989, 5, 247-275.

15. Snyder, D.S., and McIntosh, T.J. The lipopolysaccharide barrier: correlation of antibiotic susceptibility with antibiotic permeability and fluorescence probe binding kinetics. Biochemistry 2000, 39 11777-11787.

16. Fischer, W. Lipoteichoic acid and lipids in the membrane of Staphylococcus aureus. Med. Microbiol. Immunol. 1994, 183, 61-76.

17. Nielsen, J.E., Bjørnestad, V.A., Pipich, V., Jenssen, H., and Lund, R. Beyond structural models for the mode of action: How natural antimicrobial peptides affect lipid transport. J. Colloid Interface Sci. 2021, 582, 793-802.

18. Schmidtchen, A., and Malmsten, M. (Lipo)polysaccharide interactions of antimicrobial peptides. J. Colloid Interface Sci. 2015, 449, 136-142.

19. Hancock, R.E.W., Haney, E.F., and Gill, E.E. The immunology of host defence peptides: beyond antimicrobial activity. Nat. Rev. Immunol. 2016, 16, 321-334.

20. Rončević, T., Puizina, J., and Tossi, A. Antimicrobial peptides as anti-infective agents in pre-post-antibiotic era? Int. J. Mol. Sci. 2019, 20, 2713:1-32.

21. Cardoso, M.H., Orozco, R.Q., Rezende, S.B., Rodrigues, G., Oshiro, K.G.N., Candido, E.S., and Franco, O.L. Computer-aided design of antimicrobial peptides: Are we generating effective drug candidates? Front. Microbiol. 2020, 10, 3097: 1-15.

22. Caselli, L., Parra-Ortiz, E., Micciulla, S., Skoda, M, et al. Boosting membrane interactions and antimicrobial effects of photocatalytic titanium dioxide nanoparticles by peptide coating. Small 2024, 2309496.

23. Caselli, L., Traini, T., Micciulla, S., Sebastiani, F., Köhler, S., Nielsen, E.M., et al. Antimicrobial peptide coating of TiO_2 nanoparticles for boosted antimicrobial effects. Advanced Functional Materials 2024, 2405047.

24. Ye, C., Li, W., Yang, Y., Liu, Q., Li, S., Zheng, P., Zheng, X., Zhang, Y., He, J., Chen, Y., Hua, L., Yang, Z., Li, D., Ren, Z., Yang, Y., Qi, J., Huang, W., and Ma, Y. Inappropriate use of antibiotics exacerbates inflammation through OMV-induced pyroptosis in MDR Klebsiella pneumoniae infection. Cell Reports 2021, 36, 109750: 1-13.

25. Reddy, K. M., Manorama, S. V., and Reddy, A. R. Bandgap studies on anatase titanium dioxide nanoparticles. Mater. Chem. Phys. 2003, 78, 239-245.
26. Dürr, U.H.N., Sudheendra, U.S., and Ramamoorthy, A. LL-37, the only human member of the cathelicidin family of antimicrobial peptides. Biochim. Biophys. Acta 2006, 1758, 1408-1425.
27. Bertani, B., Ruiz, N. Function and biogenesis of lipopolysaccharides. EcoSal Plus 2018, 8, 1: 1-33.
28. Caroff, M., Novikov, A. Lipopolysaccharides: structure, function and bacterial identification. OCL 2020, 27, 31: 1-10.
29. Percy, M.G., Gründling, A. Lipoteichoic acid synthesis and function in Gram-positive bacteria. Ann. Rev. Microbiol. 2014, 68, 81-100.
30. Lamberts, H., Piessens, S., Bloem, A., Pronk, H., and Finkel, P. Natural skin surface pH is on average below 5, which is beneficial for its resident flora.Int. J. Cosmet. Sci, 20016, 28, 359-370.
31. Proksch, E. pH in nature, humans, and skin. J. Dermatol. 20218, 45, 1044-1052.
32. Percival, S.L., McCarty, S., Hunt, J.A., and Woods, E.J. The effects of pH on wound healing, biofilms, and antimicrobial activity. Wound. Rep. Regen. 2014, 22, 174-186.
33. Malekkhaiat Häffner, S., Parra-Ortiz, E., Skoda, M.W.A., Saerbeck, T., Browning, K.L., and Malmsten, M. Composition effects on photooxidative membrane destabilization. J. Colloid Interface Sci. 2021, 584, 19-33.
34. Parra-Ortiz, E., Malekkhaiat Häffner, S., Saerbeck, T., Skoda, M.W.A., Browning, K.L., and Malmsten, M. Oxidation of polyunsaturated lipid membranes by photocatalytic titanium dioxide nanoparticles: role of pH and salinity. ACS Appl. Mater. Interf. Sci. 2020, 12, 32446-32460.
35. Parra-Ortiz, E., Caselli, L., Agnoletti, M., Skoda, M.W.A., Li, X., Zhao, D., and Malmsten, M. Mesoporous silica as a matrix for photocatalytic titanium dioxide nanoparticles: Lipid membrane interactions. Nanoscale 2022, 14, 12297-12312.
36. Ahn, H. J., Kim, K. I., Kim, G., Moon, E., Yang, S.S., and Lee, J.-S. Atmospheric-pressure plasma jet induces apoptosis involving mitochondria via generation of free radicals. PLoS One 2011, 6, e28154:1-7.
37. Fang, G.-D., Dionysiou, D.D., Al-Abed, S.R., and Zhou, D.-M. Superoxide radical driving the activation of persulfate by magnetite nanoparticles: implications for the degradation of PCBs. Appl. Catal., B 2013, 129, 325-332.
38. Schneider, C.A., Rasband, W.S., and Eliceiri, K.W. NIH Image to ImageJ: 25 years of image analysis. Nature Methods 2012, 9, 7, 671–675.

39. Collins, T.J. ImageJ for microscopy. BioTechniques 2007, 43 (1 Suppl), 25–30.
40. Pernot, P., Theveneau, P., Giraud, T., Fernandes, R. N., Nurizzo, D., Spruce, D., Surr, J., McSweeney, S., Round, A., Felisaz, F., Foedinger, L., Gobbo, A., Huet, J., Villard, C., and Cipriani, F. New beamline dedicated to solution scattering from biological macromolecules at the ESRF. Journal of Physics: Conference Series 2010, 247, 012009.
41. Incardona, M. F., Bourenkov, G. P., Levik, K., Pieritz, R. A., Popov, A. N., and Svensson, O. EDNA: a framework for plugin-based applications applied to X-ray experiment online data analysis. Journal of synchrotron radiation 2009, 16, 872-879.
42. Good, R. J., and E. D. Kotsidas. The contact angle of water on polystyrene: a study of the cause of hysteresis. Journal of Colloid and Interface Science 1978, 66, 360-362.
43. Ellison, A. H., and W. A. Zisman. Wettability studies on nylon, polyethylene terephthalate and polystyrene. The Journal of Physical Chemistry 1954, 58, 503-506.
44. Singh, S., Kalle, M., Papareddy, P., Schmidtchen, A., and Malmsten, M. Lipopolysaccharide interactions of C-terminal peptides from human thrombin. Biomacromolecules 2013, 14, 1482-1492.
45. Cubitt, R., and Fragneto, G. D17: The new reflectometer at the ILL. Appl Phys A-Mater 2002, 74, 329-331.
46. Saerbeck, T., Cubitt, R., Wildes, A., Manzin, G., Andersen, K.H., and Gutfreund, P. Recent upgrades of the neutron reflectometer D17 at ILL. J Appl Cryst 2018, 51, 249-256.
47. Webster, J. R. P., Langridge, S., Dalgliesh, R. M., and Charlton, T. R. Reflectometry techniques on the Second Target Station at ISIS: Methods and science. The European Physical Journal Plus 2011, 126, 112.
48. Rodriguez-Loureiro, I., Latza, V. M., Fragneto, G., Schneck, E. Conformation of Single and Interacting Lipopolysaccharide Surfaces Bearing O-Side Chains. Biophysical Journal 2018, 114, 7, 1624-1635
49. Wang, M., Liechti, K. M., Wang, Q., and White, J. M. Self-Assembled Silane Monolayers: Fabrication with Nanoscale Uniformity. Langmuir 2005, 21, 5, 1848–1857.
50. Carson, G. A., and Granick, S. Self-assembly of octadecyltrichlorosilane monolayers on mica. Journal of Materials Research 1990, 5, 1745-1751.
51. Sanket, K. S., Chiavetta, D., and Wolden, C. A. Formation of octadecyltrichlorosilane (OTS) self-assembled monolayers on amorphous alumina. Applied surface science 2013, 282, 291-296.
52. Nelson, A. Motofit – integrating neutron reflectometry acquisition, reduction and analysis into one, easy to use, package. J. Phys. Conf. Ser. 2010, 251, 012094.

53. Nelson, A. Co-refinement of multiple contrast neutron / X-ray reflectivity data using MOTOFIT. J. Appl. Cryst. 2006, 39, 273-276.
54. Heinrich, F., Ng, T., Vanderah, D.J., Shekar, P., Mihailescu, M., Nanda, H., and Lösche, M. A new lipid anchor for sparsely tethered bilayer lipid membranes. Langmuir 2009, 25, 4219-4229.
55. Kosmulski, M. pH-dependent surface charging and points of zero charge: III. Update. J. Colloid Interface Sci. 2006, 298, 730-741.
56. Kosmulski, M. The significance of the difference in the point of zero charge between rutile and anatase. Adv. Colloid Interface Sci. 2002, 99, 255-264.
57. Davies, M.J. The oxidative environment and protein damage. Biochim. Biophys. Acta 2005, 1703, 93-109.
58. Singh, S., Papareddy, P., Kalle, M., Schmidtchen, A., and Malmsten, M. Importance of lipopolysaccharide disruption for the anti-endotoxic effects of heparin cofactor II peptides. Biochim. Biophys. Acta 2013, 1828, 2709-2719.
59. Bello, G., Eriksson, J., Terry, A., Edwards, K., Lawrence, M.J., Barlow, D, and Harvey, R.D. Characterization of the aggregates formed by various bacterial lipopolysaccharides in solution and upon interaction with antimicrobial peptides. Langmuir 2015, 31, 741-751.
60. Castelletto, V., Seitsonen, J., and Hamley, I. W. Effect of Glycosylation on Self-Assembly of Lipid A Lipopolysaccharides in Aqueous Solutions. Langmuir 2023, 39, 24, 8516–8522.
61. Redeker, C., and Briscoe, W. H. Interactions between Mutant Bacterial Lipopolysaccharide (LPS-Ra) Surface Layers: Surface Vesicles, Membrane Fusion, and Effect of Ca2+ and Temperature. Langmuir 2019, 35, 48, 15739–15750.
62. Tong, J., and McIntosh, T. J. Structure of Supported Bilayers Composed of Lipopolysaccharides and Bacterial Phospholipids: Raft Formation and Implications for Bacterial Resistance. Biophysical Journal 2004, 86, 6, 3759-3771.
63. Paracini, N., Clifton, L. A., Skoda, M. W. A., and Lakey, J. H. Liquid crystalline bacterial outer membranes are critical for antibiotic susceptibility. PNAS 2018, 115, 32, E7587-E7594
64. Hong, L., Gontsarik, M., Amenitsch, H., and Salentinig, S. Human Antimicrobial Peptide Triggered Colloidal Transformations in Bacteria Membrane Lipopolysaccharides. Small 2022, 18, 5, 2104211.
65. McConnell, K.I., Shamsudeen, S., Meraz, I.M., Mahadevan, T.S., Ziemys, A., Rees, P., Summers, H.D., and Serda, R.E. Reduced cationic nanoparticle toxicity based on serum masking of surface potential. J. Biomed. Nanotechnol. 2016, 12, 154-164.

66. Weiss, M., Fan, J., Claudel, M., Sonntag, T., Didier, P., Ronzani, C., Lebeau, L., and Pons, F. Density of surface charge is a more predictive factor of the toxicity of cationic carbon nanoparticles than zeta potential. J. Nanobiotechnol. 2021, 19, 5: 1-18.

67. Malekkhaiat-Häffner S, Nyström L, Browning K, Mørck Nielsen H, Strömstedt A, van der Plas M, Schmidtchen A, Malmsten M: Interaction of laponite with membrane components – consequences for bacterial aggregation and infection confinement. ACS Appl. Mater. Interf. 2019, 11, 15389-15400.

68. Malekkhaiat Häffner, S., Nyström, L., Strömstedt, A.A., Li, L., van der Plas, M.J.A., and Malmsten, M. Nanoclay-induced bacterial flocculation for infection confinement. J. Colloid Interface Sci. 2020, 562, 71-80.

69. Duong, D.T., Singh, S., Bagheri, M., Verma, N.K., Schmidtchen, A., and Malmsten, M. Pronounced peptide selectivity for melanoma through tryptophan end-tagging. Sci. Rep. 2016, 6, 24952:1-17.

70. Lu, Z., Dai, T., Huang, L., Kurup, D.B., Tegos, G.P., Jahnke, A., Wharton, T., and Hamblin, M.R. Photodynamic therapy with a cationic functionalized fullerene rescues mice from fatal wound infections. Nanomedicine 2010, 5, 1525-1533.

71. Zhang, Y., Zhang, H., Zou, Q., Xing, R., Jiao, T., and Yan, X. An injectable dipeptide-fullerene supramolecular hydrogel for photodynamic antibacterial therapy. J. Mater. Chem. B 2018, 6, 7335-7342.

72. Chen, H., Zhang, M., Li, B., Chen, D., Dong, X., Wang, Y., and Gu, Y. Versatile antimicrobial peptide-based ZnO quantum dots for in vivo bacteria diagnosis and treatment with high specificity. Biomaterials 2015, 53, 532-544.

73. Kurz, J., Eberle, F., Graumann, T., Kaschler, M.-E., Sähr, A., Neumann, F., Dalpke, A.H., and Erdinger, L. Inactivation of LPS and RNase A on photocatalytically active surfaces. Chemosphere 2011, 84, 1188-1193.

74. Neacsu, P., Mazare, A., Schmuki, P., and Cimpean, A. Attenuation of the macrophage inflammatory activity of TiO2 nanotubes via inhibition of MAPK and NF-□B pathways. Int. J. Nanomed. 2015, 10, 6455-6467.

75. Cruz Gomes da Silva, R. L., Oliveira da Silva, H. F., da Silva Gasparotto, L. H., Caseli, L. How the interaction of PVP-stabilized Ag nanoparticles with models of cellular membranes at the air-water interface is modulated by the monolayer composition. Journal of Colloid and Interface Science 2018, 512, 792-800.

76. An, X., Naowarojna, N., Liu, P., and Reinhard, B.M. Hybrid plasmonic photoreactors as visible light-mediated bactericides. ACS Appl. Mater. Interf. 2020, 12, 106-116.
77. Kiwi, J., and Nadtochenko, V. Evidence for the mechanism of photocatalytic degradation of the bacterial wall membrane at the TiO2 interface by ATR-FTIR and laser kinetic spectroscopy. Langmuir 2005, 21, 463-4641.
78. Liu, P., Duan, W., and Li, X. The damage of outer membrane of Eschericha coli in the presence of TiO2 combined with UV light. Colloid Surf. B 2010, 78, 171-176.
79. Engel, M., Hadar, Y., Belkin, S., Lu, X., Elimelech, M., and Chefetz, B. Bacterial inactivation by a carbon nanotube-iron oxide nanocomposite: a mechanistic study using E. coli mutants. Environ. Sci. 2018, 5, 372-380.
80. Petrlova, J., Hansen, F.J., van der Plas, M.J.A., Huber, R.G., Mörgelin, M., Malmsten, M., Bond, P.J., and Schmidtchen, A. Aggregation of thrombin-derived C-terminal fragments – a novel host defense mechanism. Proc. Natl. Acad. Sci. USA 2017, 114, E4213-E4222.

Photocatalytic degradation of bacterial lipopolysaccharides by peptide-coated TiO_2 nanoparticles

Lucrezia Caselli,[1,] Guanqun Du[1], Samantha Micciulla[2], Tanja Traini[3], Federica Sebastiani[1,3], Ragna Guldsmed Diedrichsen[3], Sebastian Köhler[4], Maximilian W. A. Skoda[5], Mariena J.A. van der Plas[3], and Martin Malmsten[1,3]*

[1]Department of Physical Chemistry 1, Lund University, SE-22100 Lund, Sweden

[2]Institut Laue–Langevin, CS 20156, 38042 Grenoble Cedex 9, France

[3]Department of Pharmacy, University of Copenhagen, DK-2100 Copenhagen, Denmark

[4]LINXS Institute of Advanced Neutron and X-ray Science, Scheelevagen 19, 22370 Lund, Sweden

[5] ISIS Pulsed Neutron and Muon Source, Rutherford Appleton Laboratory, OX11 0QX, Harwell, UK

[*]Corresponding author

KEYWORDS: Antimicrobial peptide, lipopolysaccharide, photocatalysis, oxidation, TiO_2

Scheme S1 Schematic illustration of the model applied to fit the NR data. For smooth LPS adsorbed on pre-coated SiO_2-OTS surfaces (in the absence as well as in the presence of NPs), a 3-layer model was employed. This comprises a single and fully interdigitated OTS/lipid A hydrophobic layer on top of the SiO_2 surface, followed by a layer of core oligosaccharides, and an outer layer of O-antigen chains.

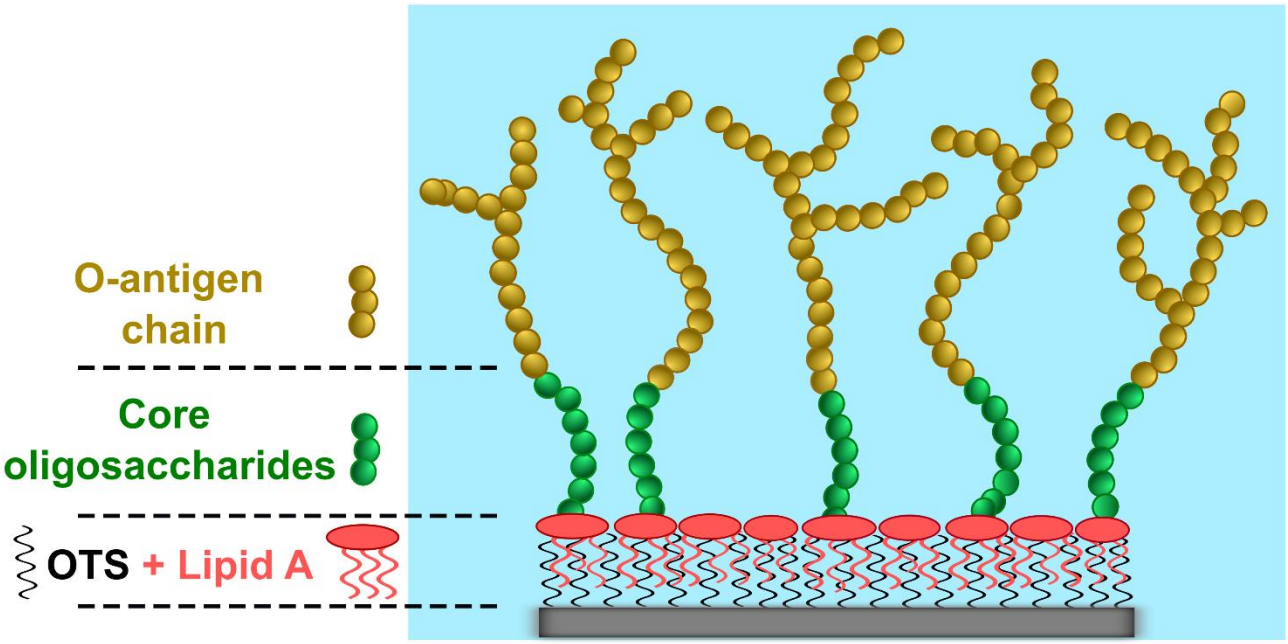

Table S1. Summary of structural data obtained from the NR fits for the hydrophobic OTS layer, pre-formed onto SiO_2 blocks. The value of the SLD of the layer is shown in bold and was assumed constant and taken from literature (1). Shown also are fitted structural parameters, including thickness (Thick), hydration (Hyd) and roughness (Rough) of the layer. These parameters were obtained fitting the NR profiles by using the Genetic Optimization method the available on the Motofit analysis package within the software IGOR Pro (2,3), according to a single layer model accounting for the OTS layer covalently bound to the SiO_2 surface. A Monte Carlo error analysis allowing for refitting data 200 times was employed to minimize the uncertainty associated to data fitting (4).

SLD (10^{-6} Å^{-2})	Thick (Å)	Hyd (vol%)	Rough (Å)
-0.35	30.9 ± 0.1	0.8 ± 0.2	5.9 ± 0.1

Table S2. Summary of structural data obtained from the NR fits for supported smooth LPS before and after **bare TiO_2** NP deposition, as well as after 2 h of UV exposure. Input parameters (i.e., SLD values for the different layers) are shown in bold, assumed constant with fixed values taken from previous studies (1,5). For core oligosaccharide and O-antigen chain layers, the variation in the SLD in the different contrasts (d-, qm- and h-buffer, i.e., 10 mM Tris buffer in 100% v/v D_2O, 68.6/31.4% v/v D_2O/H_2O, and 100% v/v H_2O, respectively) due to partial hydrogen exchange was considered according to previous studies (1,5). Additionally, the SLD of the mixed OTS/Lipid A layer was taken as the arithmetic mean of OTS and lipid A individual components. Shown also are calculated structural parameters, including thickness (Thick), hydration (Hyd, referring to volume percentage), roughness (Rough) for each layer. These parameters were obtained fitting the NR profiles by using the Genetic Optimization method the available on the Motofit analysis package within the software IGOR Pro (2,3), according to a 3-layers model (**Scheme S1**), which accounts for: (1) a fully interdigitated OTS/Lipid A layer, (2) a core oligosaccharide layer, and (3) an outer layer of O-antigen chains. A Monte Carlo error analysis allowing for refitting data 200 times was employed to minimize the uncertainty associated to data fitting (4). Data taken from (6).

	SLD (10^{-6} Å^{-2})	Thick (Å)	Hyd (vol %)	Rough (Å)
OTS + Lipid A				
Initial	**-0.37** (OTS=**-0.35** Lipid A=**--0.4)**	32.8 ± 0.2	0.06 ± 0.05	4.9 ± 0.2
TiO_2		29.2 ± 0.2	0.4 ± 0.2	6.4 ± 0.3
+2h UV		30.1 ± 0.1	0.4 ± 0.2	5.4 ± 0.3
Core oligosaccharides				
Initial	**1.85** (h) **3.79** (qm) **4.70** (d)	10.2 ± 0.2	47 ± 3	4.1 ± 0.1
TiO_2		14 ± 2	47 ± 7	4.6 ± 0.3
+2h UV		13 ± 1	45 ± 6	5.3 ± 0.4
O-antigen chain				
Initial	**1.57** (h) **3.19** (qm) **3.94** (d)	103 ± 9	97 ± 1	5.3 ± 0.2
TiO_2		106 ± 12	95 ± 3	8 ± 1
+2h UV		84 ±17	96 ± 1	8 ± 1

Table S3. Summary of structural data obtained from the NR fits for supported smooth LPS before and after **LL-37-TiO$_2$** NP deposition, as well as after 2 h of UV exposure. Input parameters (i.e., SLD values for the different layers) are shown in bold, assumed constant with fixed values taken from previous studies (1,5). For core oligosaccharide and O-antigen chain layers, the variation in the SLD in the different contrasts (d-, qm- and h-buffer, i.e., 10 mM Tris buffer in 100% v/v D_2O, 68.6/31.4% v/v D_2O/H_2O, and 100% v/v H_2O, respectively) due to partial hydrogen exchange was considered according to previous studies (1,5). Additionally, the SLD of the mixed OTS/Lipid A layer has been taken as the arithmetic mean of OTS and lipid A individual components. Shown also are calculated structural parameters, including thickness (Thick), hydration (Hyd, referring to volume percentage), roughness (Rough) for each layer. These parameters were obtained fitting the NR profiles by using the Genetic Optimization method the available on the Motofit analysis package within the software IGOR Pro (2,3), according to a 3-layers model (**Scheme S1**), which accounts for: (1) a fully interdigitated OTS/Lipid A layer, (2) a core oligosaccharide layer, and (3) an outer layer of O-antigen chains. A Monte Carlo error analysis allowing for refitting data 200 times was employed to minimize the uncertainty associated to data fitting (4).

	SLD (10^{-6} Å^{-2})	Thick (Å)	Hyd (vol %)	Rough (Å)
OTS + Lipid A				
Initial	**-0.37** (OTS=**-0.35** Lipid A=**--0.4)**	27.8 ± 0.1	0.5 ± 0.3	6.5 ± 0.2
LL-37-TiO_2		28.3 ± 0.1	0.3 ± 0.2	7.3 ± 0.1
+2h UV		27.8 ± 0.2	0.6 ± 0.2	5.1 ± 0.1
Core oligosaccharides				
Initial	**1.85** (h) **3.79** (qm) **4.70** (d)	16.3 ± 0.8	34 ± 3	5 ± 0.3
LL-37-TiO_2		14.2 ± 05	32 ± 2	4.2 ± 0.1
+2h UV		10 ± 1	36 ± 5	6.7 ± 0.2
O-antigen chain				
Initial	**1.57** (h) **3.19** (qm) **3.94** (d)	124 ± 24	97 ± 1	9 ± 1
LL-37-TiO_2		40 ± 7	94.3 ± 0.7	5.7 ± 0.4
+2h UV		9 ± 1	59 ± 8	10 ± 1

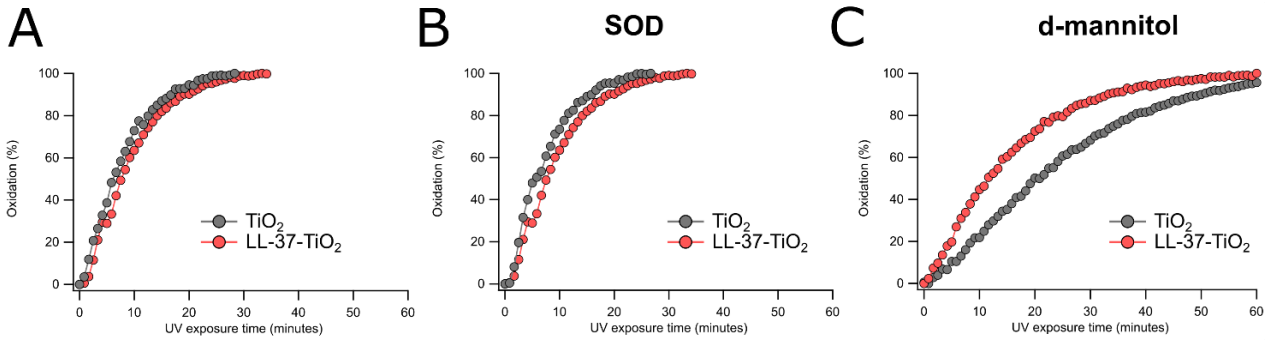

Figure S1. Representative C_{11}-BODIPY oxidation kinetics, showing effects of 100 ppm bare TiO_2 NPs (grey) and LL-37-TiO_2 NPs (red) on +PG LUVs subjected to *in situ* UV exposure in the absence (A), and presence of SOD ($\bullet O_2^-$ scavenger, +50 U/mL) (B), ord-mannitol ($\bullet$OH scavenger, 500 mM) (C) in 10 mM Tris, pH 7.4. (n=3).

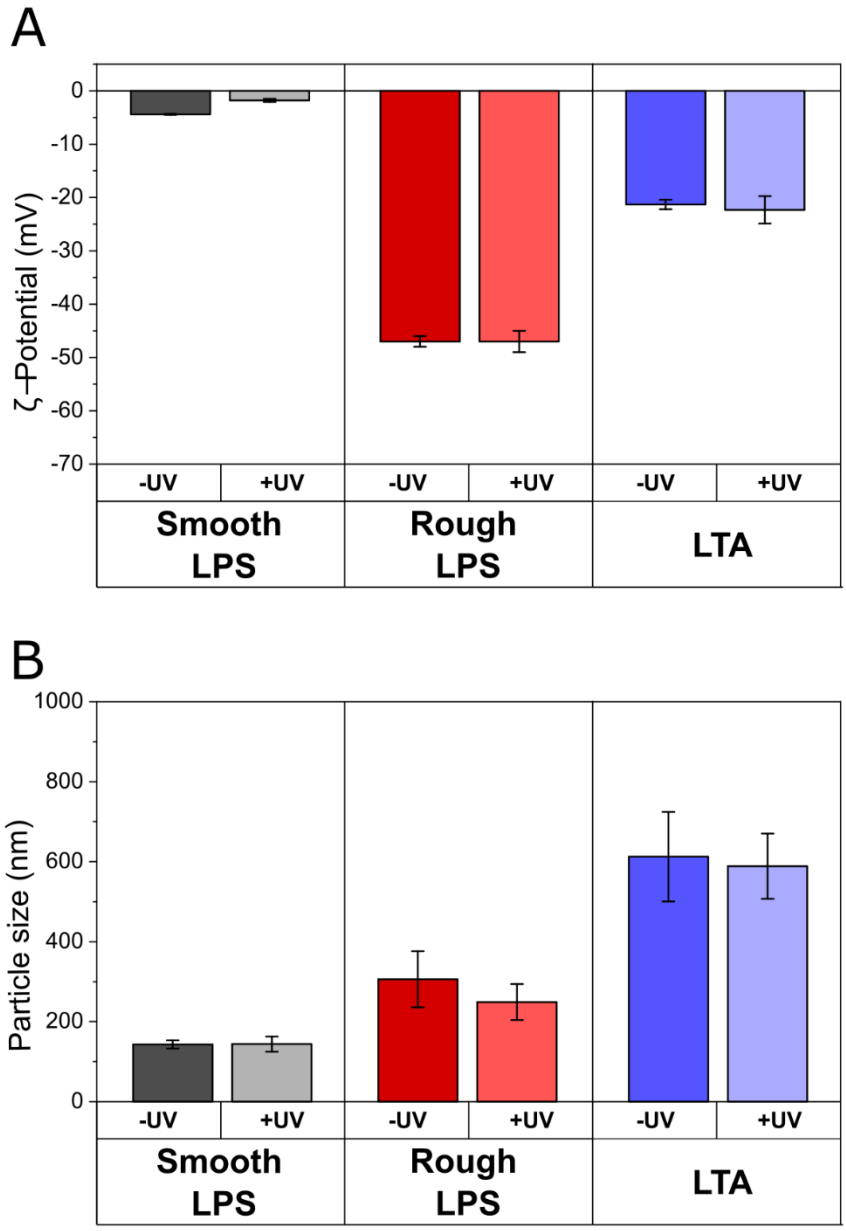

Figure S2. ζ-potential (A) and average particle size (B) for 100 ppm smooth LPS (left), rough LPS (middle), or LTA (right) in the absence of bare TiO_2 NPs, before and after 2 h of UV illumination in 10 mM Tris, pH 7.4. (n=3).

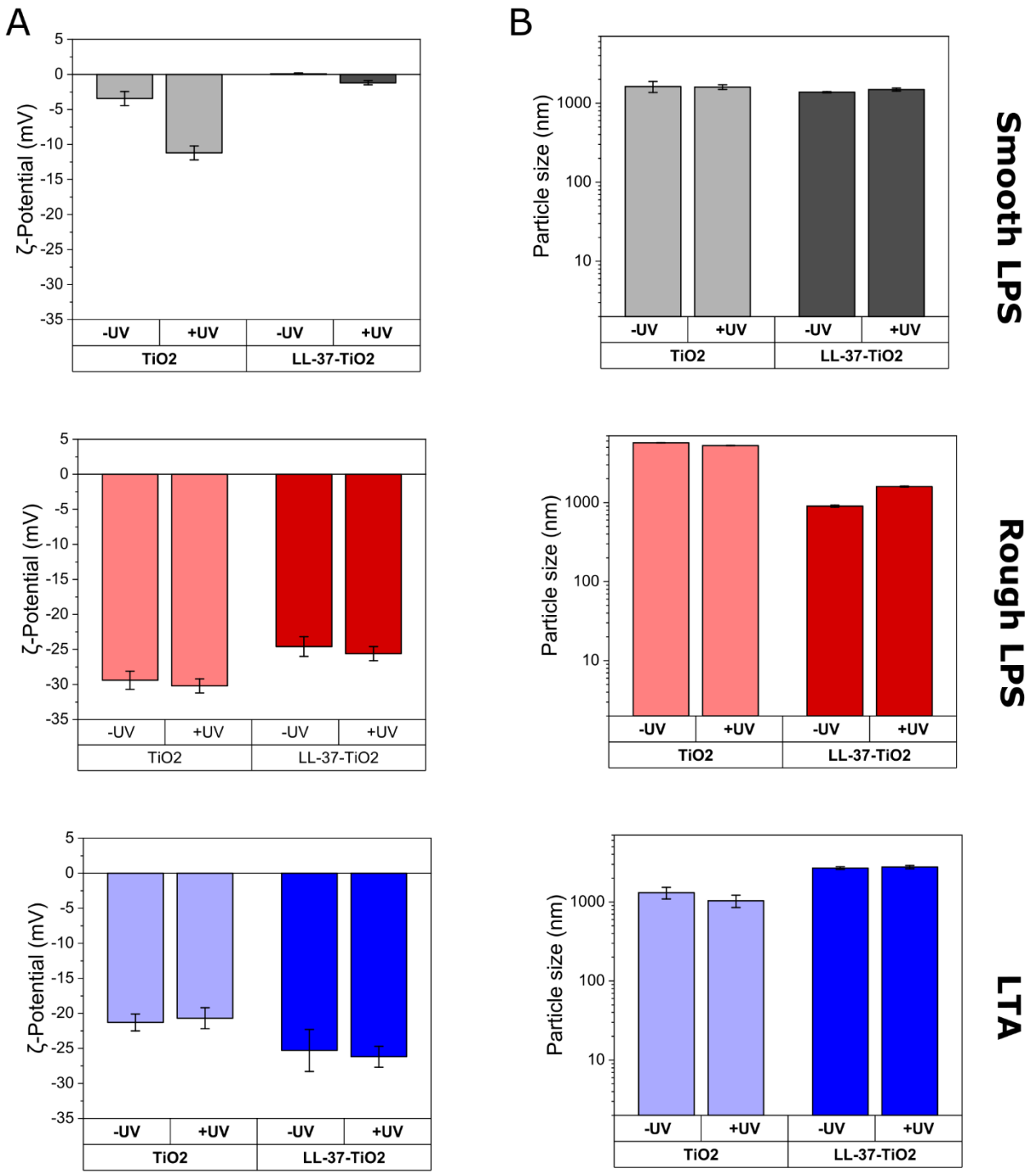

Figure S3. ζ-potential (A) and average particle size (B) obtained on mixing 100 ppm bare or LL-37-TiO_2 NPs with 100 ppm smooth LPS (top), rough LPS (middle), or LTA (bottom), as well as effects of UV illumination for 2 h in 10 mM Tris, pH 7.4. (n=3)

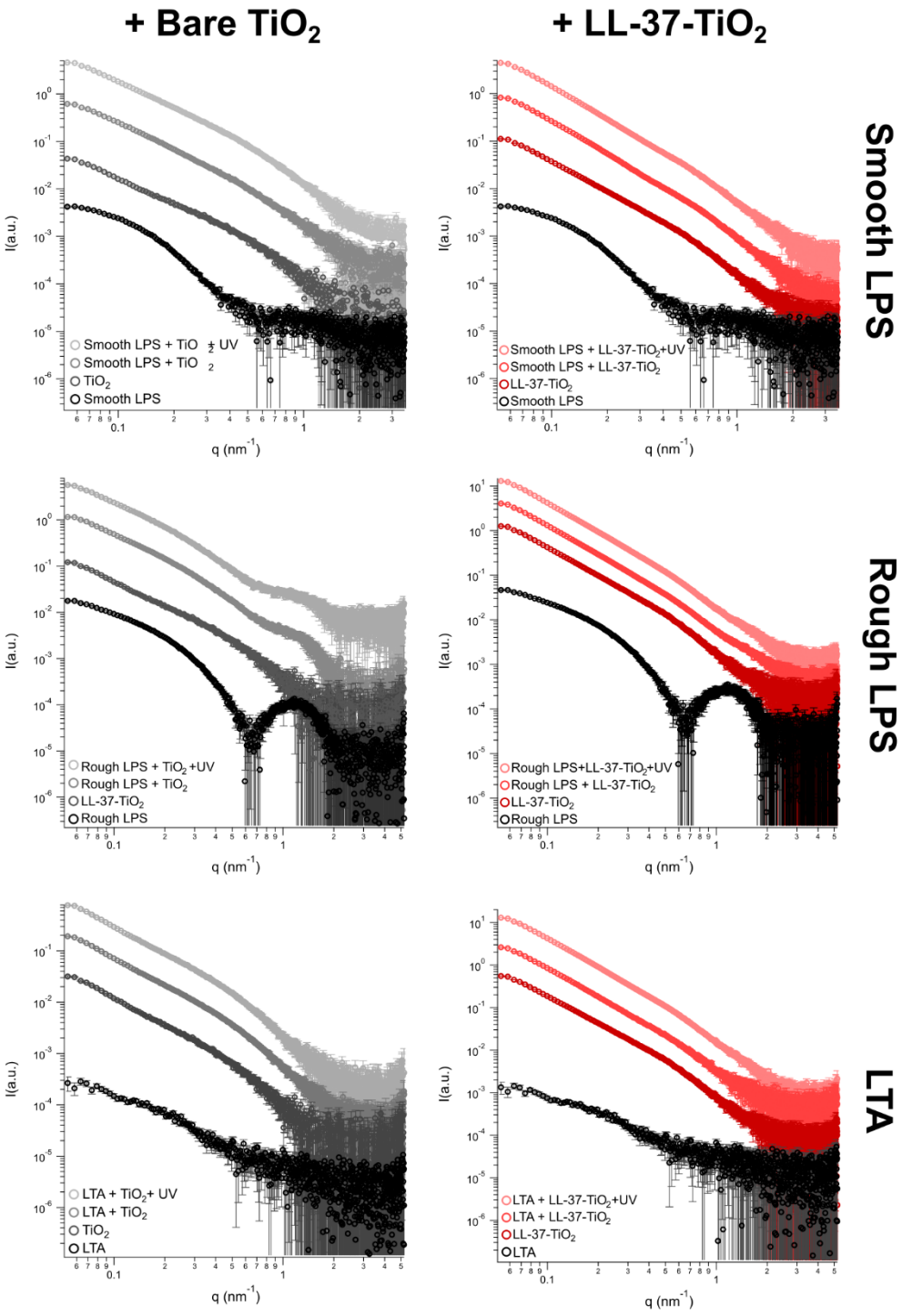

Figure S4. SAXS profiles of 100 ppm smooth LPS (top), rough LPS (middle) and LTA (bottom) incubated for 2 h with either bare (left) or LL-37-coated TiO_2 NPs (100 ppm) in the absence or presence of UV illumination, in 10 mM Tris, pH 7.4. SAXS profiles of bare LPS and LTA, as well as bare or LL-37-coated TiO_2 NPs in the same buffer, are also included as control samples. Measurements were performed at 25°C.

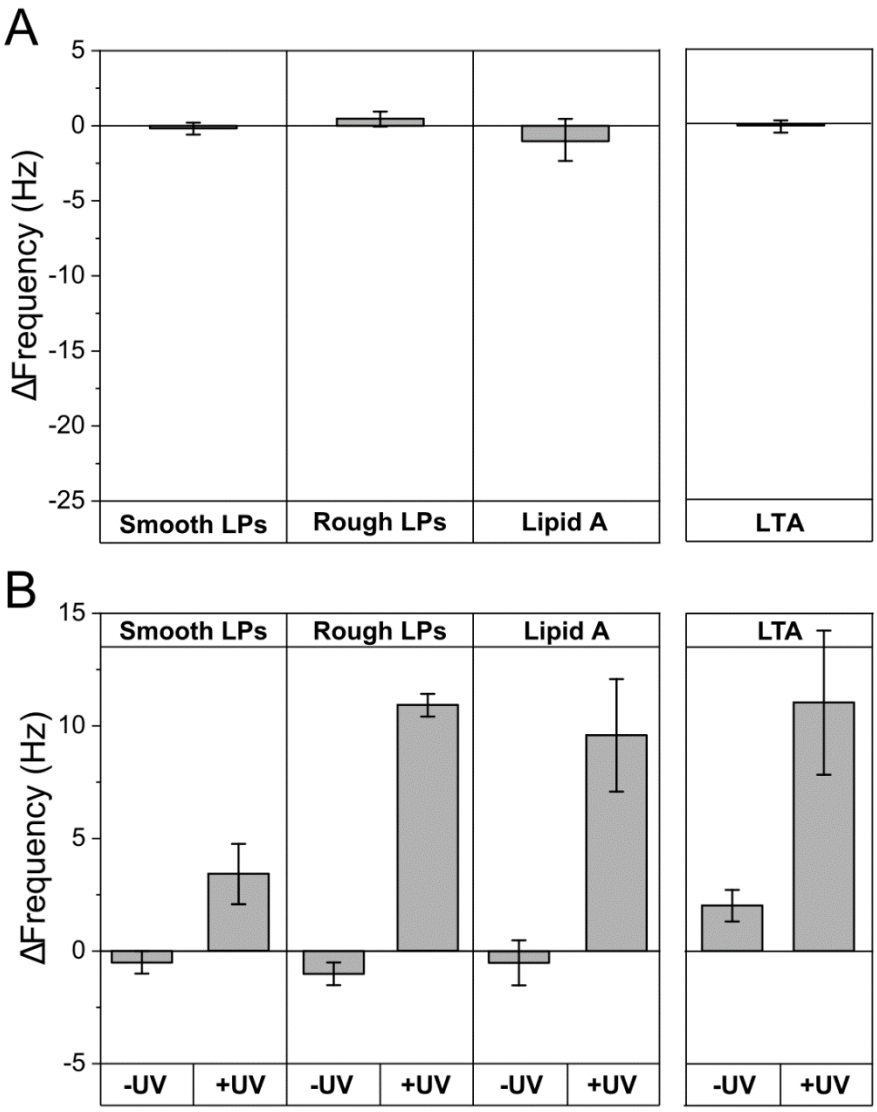

Figure S5. QCM-d results on (A) adsorption of 100 ppm of bare TiO_2 NPs to hydrophobic polystyrene surfaces coated with smooth LPS, rough LPS, lipid A and LTA (prepared as in **Figure 4**). Shown in (B) are results on the subsequent oxidative degradation of such layer after 2 hours of UV illumination. ΔF=0 corresponds to the Frequency shift for the smooth LPS, rough LPS and Lipid A layers right before NP binding (A) or UV illumination (B). Measurements were performed in 10 mM Tris, 150 mM NaCl, pH 7.4 (n=3).

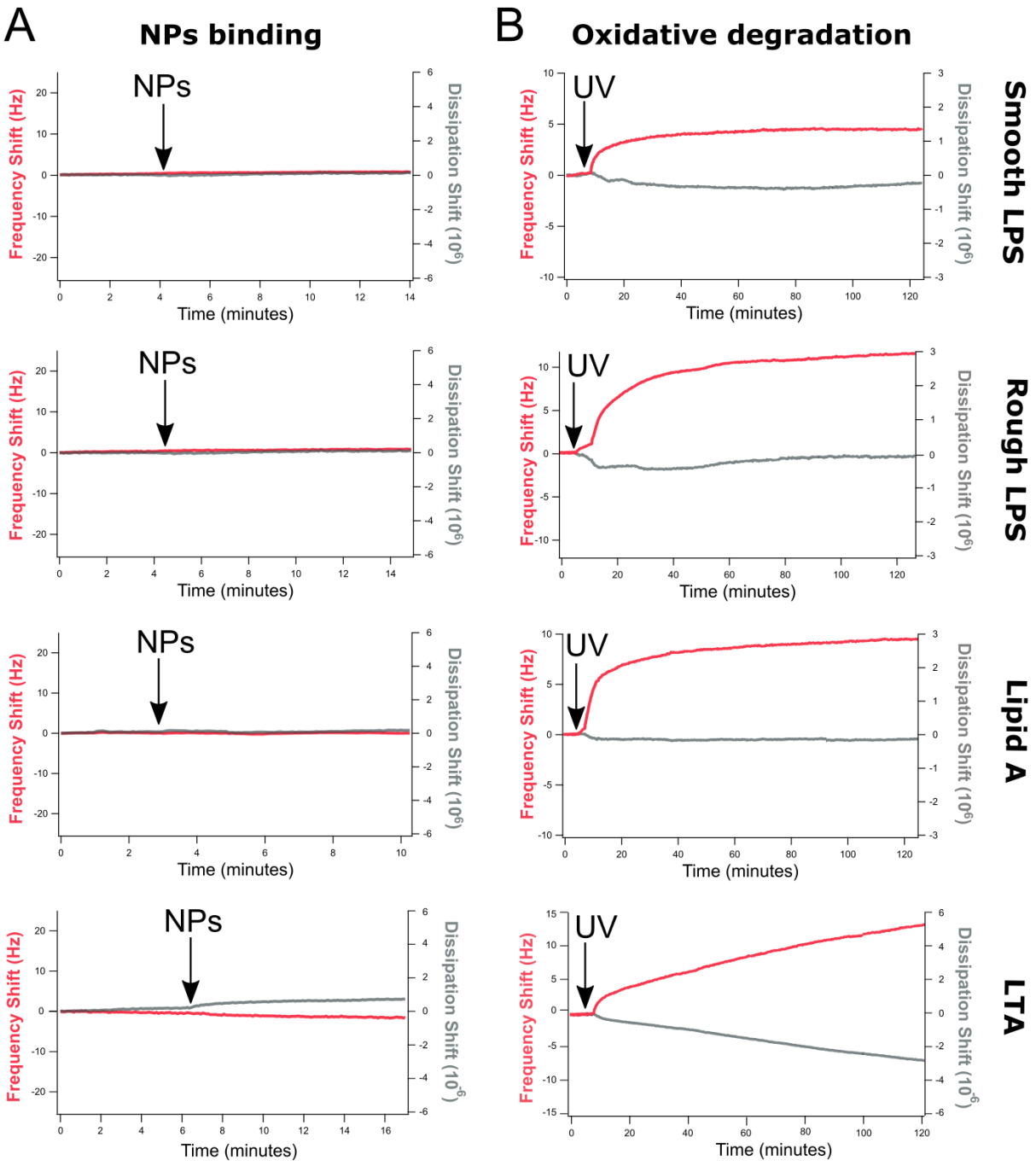

Figure S6. Representative QCM-d profiles showing the 7th overtone of ΔFrequency (Hz) and ΔDissipation ($\cdot 10^{-6}$) for (A) 100 ppm **bare TiO_2** NPs binding to smooth LPS, rough LPS, lipid A, and LTA adsorbed on polystyrene and (B) subsequent oxidative degradation induced upon UV illumination applied for 2 hours (right). ΔF=0 and ΔD=0 correspond to Frequency and Dissipation shifts for smooth LPS, rough LPS, lipid A and LTA layers right before NP binding (A) or UV illumination (B). Measurements were performed in 10 mM Tris, 150 mM NaCl, pH 7.4 (n=3).

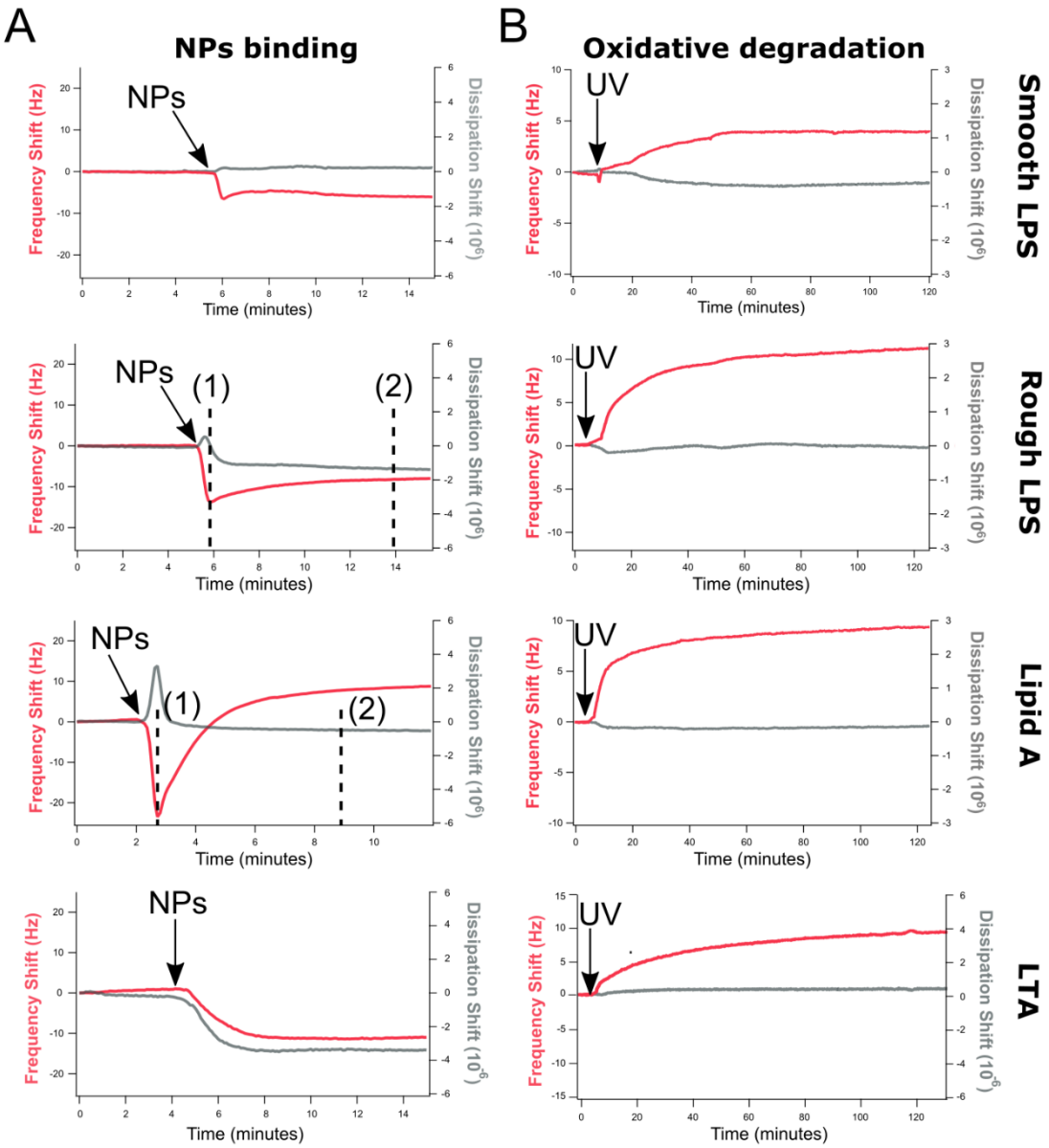

Figure S7. Representative QCM-d ΔFrequency (Hz) and ΔDissipation ($\cdot 10^{-6}$) profiles showing (A) 100 ppm **LL-37-TiO$_2$** NPs binding to smooth LPS, rough LPS, lipid A, and LTA adsorbed on polystyrene and (B) subsequent oxidative degradation induced upon UV illumination applied for 2 hours (right). ΔF=0 and ΔD=0 correspond to Frequency and Dissipation shifts for smooth LPS, rough LPS, lipid A and LTA layers right before NP binding (A) or UV illumination (B). Measurements were performed in 10 mM Tris, 150 mM NaCl, pH 7.4 (n=3). When LL-37-coated TiO_2 NPs are injected into the measurement chamber (left), a minimum in ΔF is reached soon after NP injection ((1)), indicating a maximum in NPs adsorption for rough LPS, and lipid A; this is followed by a slower increase in ΔF, consistent with a partial removal of material, which stops within 10 minutes of incubation ((2)).

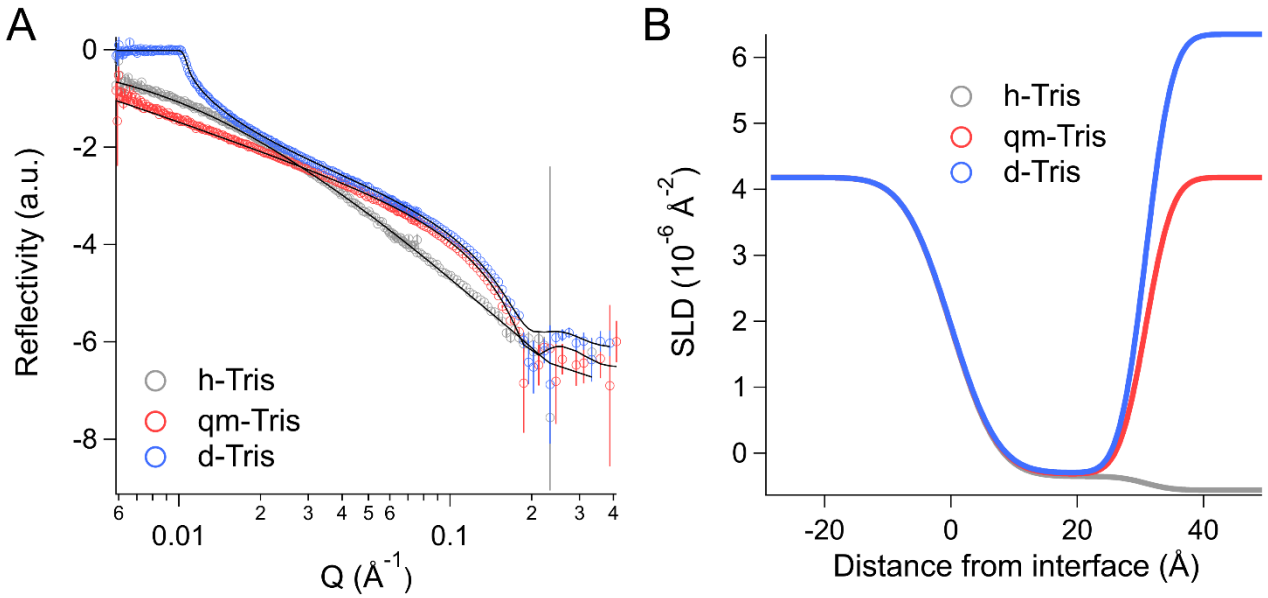

Figure S8. Neutron reflectivity curves with best model fits (A) and corresponding SLD profiles (B) for a supported OTS layer before LPS deposition in 10 mM d-Tris, qm-Tris, and h-Tris, pH 7.4. Adapted from (6).

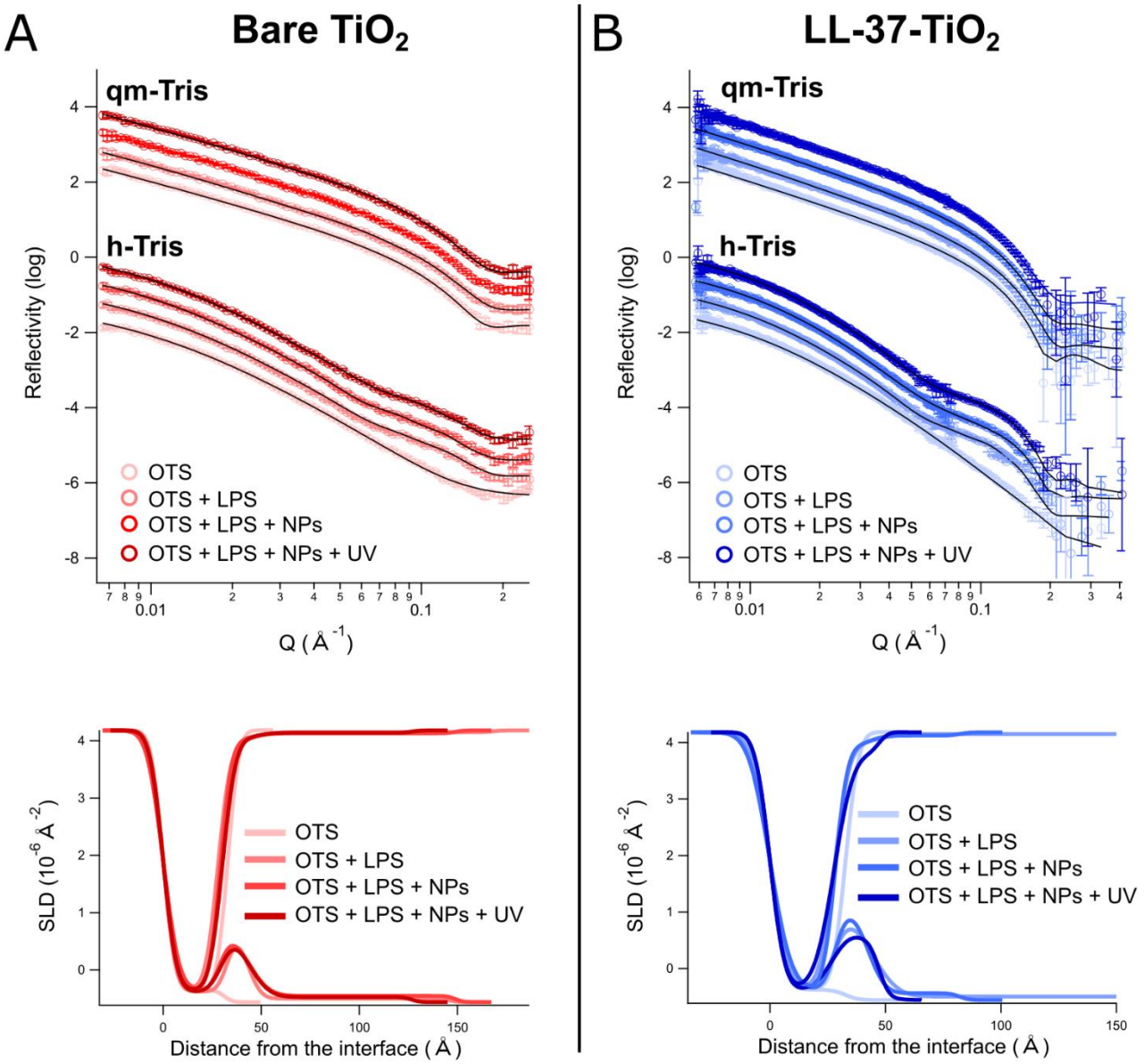

Figure S9. Neutron reflectivity curves with best model fits (upper) and corresponding SLD profiles (lower) for smooth LPS layers before and after incubation with bare TiO_2 NPs (A) and LL-37-TiO_2 NPs (B). Shown are also reflectivity curves with best model fits and SLD profiles for the corresponding systems after 2 h of *in situ* UV exposure. All experiments were performed in 10 mM Tris buffer, pH 7.4, at a nanoparticle concentration of 100 ppm. Curves are shown for two different buffer contrasts, h-tris and qm-Tris, and data for the latter are offset by $3 \cdot 10^{-1}$ for clarity. The grey box in the SLD profiles indicates the position of the silicon block and reflecting interface, consisting of bulk Si and a SiO_2 layer. Data for bare TiO_2 NPs (A panel) are adapted from (6).

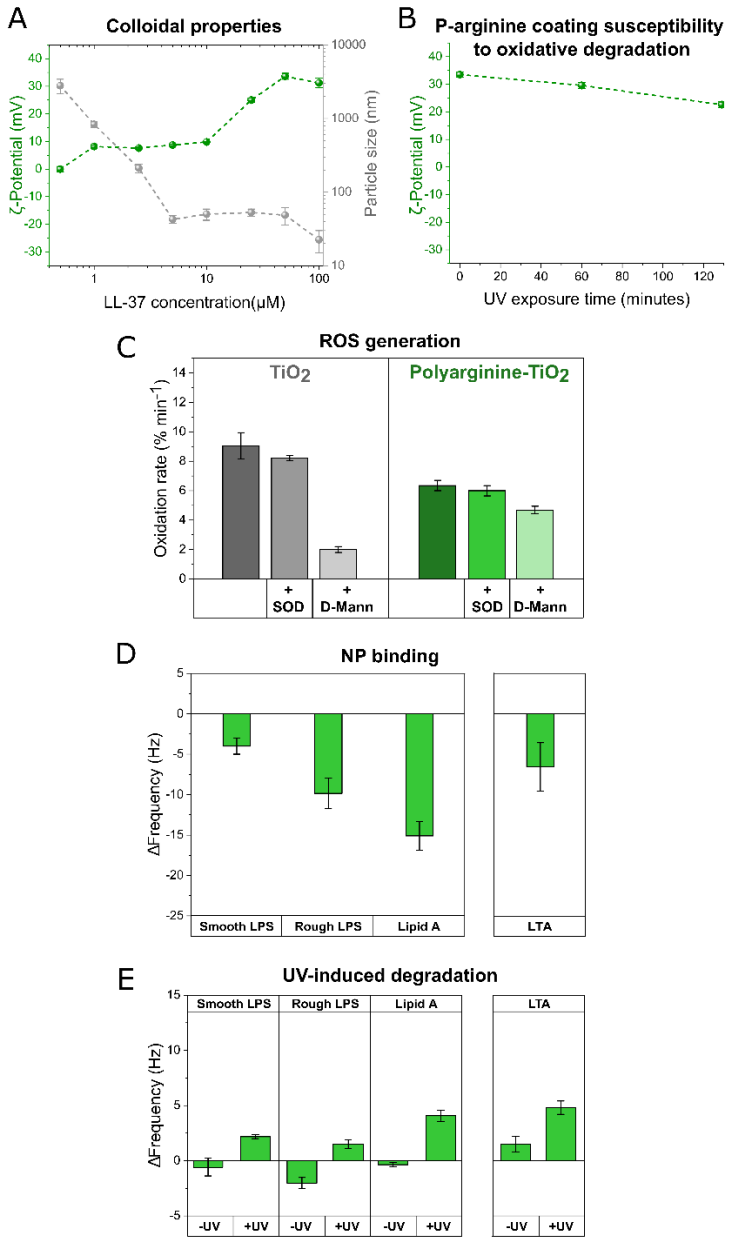

Figure S10. Concept generalization. (A) On coating TiO_2 NPs by highly positively charged polyarginine at pH 7.4, colloidal stability is strongly improved. (B) The peptide coating displays good integrity on UV exposure for 1-2 h (as inferred from the ζ-potential of polyarginine-TiO_2 NPs) and does not detrimentally interfere with ROS generation. As a result, binding of polyarginine-TiO_2 NPs to smooth LPS, rough LPS, lipid A, and LTA was strongly promoted (D). Oxidative degradation under UV exposure was comparable for smooth LPS, rough LPS, lipid A, and LTA, but smaller throughout for polyarginine-TiO_2 NPs (E) than for LL-37-TiO_2 NPs (**Figure 5B**).

References

1. Rodriguez-Loureiro, I., Latza, V.M., Fragneto, G. and Emanuel Schneck and and Schneck, E. Conformation of Single and Interacting Lipopolysaccharide surfaces bearing O-side chains. Biophys J. 2018, 116, 114, 1624-1635.

2. Nelson, A. Motofit – integrating neutron reflectometry acquisition, reduction and analysis into one, easy to use, package. J. Phys. Conf. Ser. 2010, 251, 012094.

3. Nelson, A. Co-refinement of multiple contrast neutron / X-ray reflectivity data using MOTOFIT. J. Appl. Cryst. 2006, 39, 273-276.

4. Heinrich, F., Ng, T., Vanderah, D.J., Shekar, P., Mihailescu, M., Nanda, H., and Lösche, M. A new lipid anchor for sparsely tethered bilayer lipid membranes. Langmuir 2009, 25, 4219-4229.

5. Micciulla, S., Gerelli, Y., and and Schneck, E. Structure and conformation of wild-type bacterial lipopolysaccharide layers at air-water interfaces. Biophys J. 2019, 116, 1259–1269.

6. Caselli, L., Traini, T., Micciulla, S., Sebastiani, F., Köhler, S., Nielsen, E. M., Guldsmed Diedrichsen, R., Skoda, M.W. A., Malmsten, M. Antimicrobial Peptide Coating of TiO_2 Nanoparticles for Boosted Antimicrobial Effects. Advanced Functional Materials 2024, 2405047.